JGR Solid Earth

RESEARCH ARTICLE
10.1029/2019JB018105

Vertical Displacements of the Amazon Basin From GRACE and GPS

L. A. Knowles[1], R. A. Bennett[1], and C. Harig[1]

[1]Department of Geosciences, University of Arizona, TucsonAZ, USA

Abstract The extent to which Gravity Recovery and Climate Experiment (GRACE)-recovered gravity anomalies can improve our understanding of Global Positioning System (GPS)-measured vertical displacements is currently uncertain. To address this issue, we compared vertical displacements measured by 23 GPS stations in the Amazon basin with displacements estimated from GRACE geopotential fields. We show that despite poor correlation ($r^2 = 0.15$) between rate estimates in GPS and GRACE-derived displacement time series, further analyses reveal low bias between annual amplitude estimates and a scaling near 1. There is higher correlation ($r^2 = 0.78$) between annual periodic motions, with near 1 to 1 agreement, but there is poor correlation ($r^2 = 0.02$) and little agreement between semiannual amplitude estimates. Subtracting GRACE displacements from the GPS time series flattens the GPS power spectra, reducing the spectral index magnitude, on average, from -1.2759 ± 0.0007 ("fractional Brownian motion") to -0.3346 ± 0.0006 ("fractional Gaussian noise"), suggesting that some fraction of the apparent GPS error correlation derives from mass loading signals that are not completely characterized by secular trends or seasonal periodic motions. From March 2011 to November 2016, we find a GPS and GRACE-derived displacement combined average uplift of the Amazon basin of 1.20 ± 0.26 mm/yr and combined average annual periodic motion of 10.22 ± 0.57 mm. Deviations from a standard trajectory model for site motion are apparent in both data sets and appear to coincide with various flooding and drought events between 2011 and 2016, which suggests that the GPS coordinate time series record displacements driven by large-scale climate oscillations.

Key Points:
- GRACE and GPS give complementary estimates of vertical displacement in the Amazon basin
- GRACE can be used to remove at least some mass loading signals from GPS time series and whiten the GPS error spectra
- Observed displacements reveal seasonal, interannual, and secular variations in mass loading

Supporting Information:
- Supporting information S1
- Supporting information S2

Correspondence to:
L. A. Knowles,
ljose@email.arizona.edu

Citation:
Knowles, L. A., Bennett, R. A., & Harig, C. (2020). Vertical displacements of the Amazon basin from GRACE and GPS. *Journal of Geophysical Research: Solid Earth*, *125*, e2019JB018105. https://doi.org/10.1029/2019JB018105

Received 27 MAY 2019
Accepted 5 FEB 2020
Accepted article online 10 FEB 2020

1. Introduction

Monitoring the Earth's changing shape and gravity field is challenging because the solid Earth is enveloped by the atmosphere and hydrosphere, which store and transport surface mass loads over a wide range of spatial and temporal scales. Two methods of accounting for changes in mass loading have emerged relatively recently and have potential for providing reliable estimates of mass loading. The first is the Global Positioning System (GPS), for which thousands of stations located around the globe are continuously tracking the motion of the Earth's surface, which deflects in response to mass loading. A second data set, designed specifically for inferring changes in mass loading, derives from the Gravity Recovery and Climate Experiment (GRACE), which uses tandem satellites to obtain precise, monthly averaged measurements of the Earth's gravity field. These measurements allow for estimation of changes in mass stored on the continents, in the atmosphere and oceans, and within ice sheets, as well as the expected deformational response of the Earth to these changes.

Combined in a joint inversion, GPS and GRACE may be able to provide more robust estimates of mass loading than could be determined from either system individually. In addition, a better understanding of how mass loading affects GPS time series has implications for GPS applications to active tectonics, glacial isostatic adjustment, and others, as well as GPS error analyses. GPS and GRACE, however, have differing characteristics that must be addressed to ensure compatibility. These aspects of the two systems must be considered before attempting a combination:

1. GPS and GRACE systems measure different physical quantities that may be related through a model of Earth's isostatic response to variations in surface mass loads. A large body of research has previously shown that Earth's response to short-period loads is well approximated using a spherically symmetric, nonrotating, elastic, and isotropic Earth model (Farrell, 1972). The model provides an explicit connection

between GPS and GRACE. Nevertheless, we must make a choice regarding which model parameter(s) to use as a basis for intercomparisons.

2. GPS and GRACE measurements generally cover different observation periods. GRACE has an observation period spanning April 2002 to June 2017, with minor outages in later years associated with battery maintenance and other instrument issues, as well as a lack of thermal control on the accelerometers after April 2011. GPS's observation period varies from station to station, with some stations extending back as far as the early 1990s or before and most still collecting measurements into the present. If deformation associated with mass variations is not steady state, then estimates for trend and seasonal motion amplitudes for either data set could depend critically on the time period of investigation.
3. Typical analyses of raw GPS carrier phase measurements batch the data to produce displacement time series with nominally daily sampling (e.g., Herring et al., 2016). In contrast, GRACE Level-2 solutions use a month of orbital observations to form an estimate of Earth's gravity field once per month (Tapley et al., 2004).
4. Both measurement systems are complex and potentially subject to a variety of temporally or spatially correlated error processes that may contribute importantly to the differences observed during intercomparison.
5. GPS measures displacement at discrete points, whereas GRACE images the gravity field with a spatial resolution of approximately 300 km. It is thus possible that GPS senses short wavelength signals that are below GRACE's resolution.

Several recent studies have compared the mass loading signals recorded by GPS and GRACE-derived displacement (GDD) time series, showing potential for joint interpretation of the two data sets, but all of these studies also reported statistically significant discrepancies. Many of these studies chose regions to perform comparisons with a large loading signal, such as the Amazon basin (Davis et al., 2004; Fu et al., 2013; Moreira et al., 2016), southeast Asia (Fu et al., 2013; Steckler et al., 2010), the Nepal Himalaya (Fu & Freymueller, 2012), southern Alaska (Fu et al., 2012), West Africa (Nahmani et al., 2012), Tibet (Pan et al., 2016), and Greenland (Bevis et al., 2012). Some studies have also compared GPS and GDD in locations with less extreme loading fluctuations (Gu et al., 2017; Tregoning et al., 2009).

Here we focus on the Amazon basin, with the goal of further assessing the level of agreement between GPS and GRACE estimates of vertical displacements driven by changes in mass loading. Our study differs from previous studies in that we seek to isolate components of the mass loading signal not captured by secular trends or perfectly periodic sinusoids with annual and semiannual periods. Like other studies, we explore the extent to which GDDs may be used to remove mass load signals from GPS time series. Our aim is to improve resolution of other nonloading-related signals and advance our understanding of the GPS error spectrum. The Amazon basin is a convenient location for our study because it experiences the largest loading variations in the world (Gloor et al., 2013), and long-running GPS stations are adequately abundant, although sparsely distributed. Moreover, mass loading is driven by the local climate system, which is vital to the health of the Amazon rainforest, a critical component of the global Earth system (e.g., Lenton et al., 2008).

While previous studies have focused on the Amazon basin as we do here, each has approached the data intercomparison challenges listed above differently. Davis et al. (2004) compared the annual amplitudes of GPS vertical coordinate time series with the annual amplitudes estimated using GRACE data at 10 stations near the Amazon basin, using time series with a duration approaching 2 yr. They found a near one-to-one correspondence between GPS and GRACE-based estimates, with the slope of the best fitting line to GPS versus GRACE amplitude data of 1.05 ± 0.09 and a corresponding y intercept of 0.1 ± 0.3. While they also simultaneously estimated semiannual amplitudes and secular trends in their estimation of model parameters, they did not include an analysis or discussion of the correspondence between those parameters. A later study by Fu et al. (2013), focused, in part, on the hydrologic loading signal in the Amazon basin. They also compared annual amplitudes from GPS and GDD time series for 16 stations and, like Davis et al. (2004), found that the two data sets produce estimates that agree with an approximately one-to-one correspondence in both the vertical and horizontal components of displacement. However, the stations used in their analysis were mostly located on the edge of the Amazon, with only one or two stations located closer to the river. More recently, Moreira et al. (2016) compared the GPS and GRACE displacement time series data products from several analysis centers for 18 GPS stations in the Amazon basin. They analyzed the month-to-month agreement among displacements, finding correlation coefficients ranging between about 0.45 to 0.99, depending

on GRACE and GPS analysis center pairs. Notably, they did not examine the agreement among parameters derived from the time series data, namely, estimates for secular trends or seasonal amplitudes.

Generally, past studies have found high levels of correlation in the overall displacement signal in GPS and GRACE. However, most comparisons of GPS and GRACE have also demonstrated that subtracting GRACE-estimated displacement signals from GPS reduces the root-mean-square error of GPS residuals by only 40–50% on average. Other studies have noted temporal correlations in GPS minus GDD time series, which may reflect a combination of noise and mass loading signal (which is typically not modeled in standard GPS postprocessing) (Gu et al., 2017; Fu et al., 2012). These results suggest that further investigation of the structure of GPS minus GDD time series is warranted. Toward this end, we seek to characterize any possible secular or periodic signals that remain after removing the GRACE signal, as well as the power spectral density of the residuals after removing the trend and seasonal components.

The first steps in our analysis address differences between the two measurement systems in terms of measurement type, observation period, and sampling rate. Once we have established a common datum, observation period, and sampling rate, we perform a time series analysis, including an assessment of residual errors relative to a best fit model for trend and periodic annual and semiannual motions. We end this manuscript with a discussion of the implications for the Amazon basin, including a consideration of the ability of GRACE to adequately characterize the mass loading signals in GPS.

2. Data Sources and Selection

We obtained the GPS coordinate time series data from the University of Nevada at Reno's Nevada Geodetic Laboratory (NGL) through their Plug and Play GPS Portal (Blewitt et al., 2018; https://geodesy.unr.edu). The locations of the 23 stations used in this study are shown in Figure 1. Despite the large forest canopy across much of the Amazon basin, the GPS stations in this study were installed in locations where the view of satellite signals is unobstructed. We acquired the daily NGL coordinate time series in the IGS08 realization of the terrestrial reference frame in geographical coordinates (east, north, and vertical) for all 23 stations in our study region, but we use only the vertical component in our analysis. Figure 1 will be a useful reference as we investigate individual stations in the following sections. Note that NAUS, PAIT, PAAT, BELE, and MAPA will be particularly useful in our analysis, as they are closest to the Amazon River and thus potentially record greater mass loading signals.

We acquired monthly GRACE geopotential fields as Stokes coefficients to spherical harmonic functions from the Center for Space Research (CSR) at the University of Texas at Austin. We start with the entire span of the GRACE Release 5 (RL05) Level-2 monthly geopotential fields (GSM), from April 2002 to June 2017. Degree one coefficients are included as calculated from Swenson et al. (2008). We also replace the degree two, order zero coefficients from GRACE with those calculated from satellite laser ranging (Cheng et al., 2013). We add back the Atmosphere and Ocean De-aliasing Level-1B model, which accounts for atmospheric and oceanic mass loading signals and is removed during level 2 processing. This is done to ensure compatibility with GPS (which includes loading from atmospheric effects). This model is represented in CSR's Release 5 Level-2 GAC coefficients.

Our reasoning for restoring the Atmosphere and Ocean De-aliasing Level-1B model correction to the GRACE Level-2 data set is that we seek to determine the usefulness of GRACE in correcting GPS observations of surface deformation caused by all surface mass loads, not only continental water loads. Separation of atmospheric loading from terrestrial water is valuable for investigations focused on variations in terrestrial water storage but introduces an additional layer of complexity that is not required for the purposes of removing mass load signals from GPS coordinate time series data. Nonetheless, we performed an analysis to assess the relative contributions of atmospheric and water mass signals to the Amazon data sets. This analysis can be found in the supporting information. The result of this analysis indicates that deformation associated with atmospheric pressure is small relative to the water loading signal. Thus, our brief interpretation of measured changes in terrestrial water in section 5 below is not appreciably affected by errors in the model for atmospheric pressure.

In order to compare GPS data with GRACE data, we must decide on a common datum. One approach would be to infer time variations in the mass loading field using GRACE and GPS independently, then compare

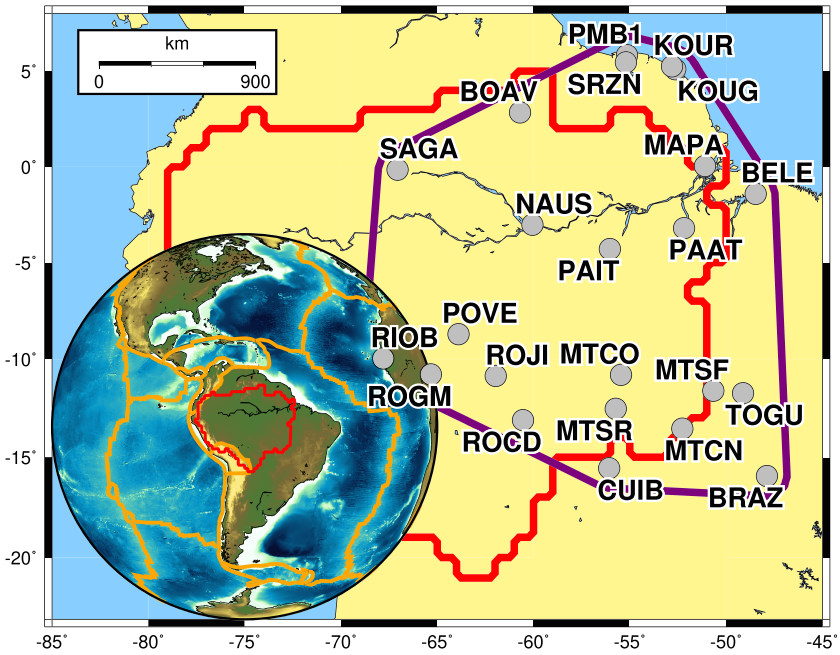

Figure 1. Map of study area with topographic inset map. Inset map has orange lines to denote plate boundaries. The border of the Amazon basin used in this study is in red in both maps. The border of the region used in our Slepian analysis is outlined in purple. The larger study area map displays the northern South American continent in yellow and the surrounding oceans in blue. The Amazon River and its tributaries (outlined in black) cut across the central and eastern parts of northern South America between about 0° and −5° latitude. The larger map also shows the locations of the 23 GPS stations, denoted by gray circles with the stations' four character IDs. Note that all 23 stations included in this study are located several hundred kilometers from the South America-Nazca and South America-Caribbean plate boundary zones.

the independently determined mass loading fields with one another. Calculating changes in mass loading is straightforward using GRACE gravity fields. However, with discrete GPS point measurements, estimation of mass loading constitutes a nonunique inverse problem (e.g., Argus et al., 2014; Borsa et al., 2014; Jin & Zhang, 2016; Wu et al., 2003). Moreover, if GPS time series data record signals that are not associated with mass loading, then changes in loading inferred from GPS could be biased. A more straightforward approach is to use the GRACE gravity fields with a suitable elastic Earth model to compute the expected displacements associated with mass load changes. These displacements can then be directly compared with GPS point measurements. In this work we adopt this latter approach, following van Dam et al. (2007), Tregoning et al. (2009), and others. This approach also permits an assessment of how well GDDs characterize the mass loading signal observed by GPS, with possible utility for improved understanding of GPS vertical coordinate time series. We will refer to time series of displacement derived from GRACE gravity anomalies as GDD time series. We will also introduce a GPS-GDD time series, formed by subtracting the GDD time series from the GPS time series.

To address the issue of differing observation periods, we restrict our analysis of GPS, GDD, and GPS-GDD time series to an overlapping period of observation. We truncate all GDD and GPS coordinate time series to a common 5 yr time period between March 2011 and November 2016. On average, this removed about 40% of the total number of GPS observations and about 60% of the total number of GRACE observations. We also limit our study to include only the 23 GPS stations in the region that have data for the (nominal) entirety of that span, with the exception of a relatively small number of missing data, presumably due to equipment maintenance. A sample time series for observed GPS-measured and GRACE-derived vertical displacements at GPS station PAAT is shown in Figure 2, illustrating their different temporal coverage and common overlapping time period. For completeness, we also show analyses of the longer GPS time series (stations BELE, BRAZ, CUIB, and KOUR) in the supporting information (Figures S1–S4).

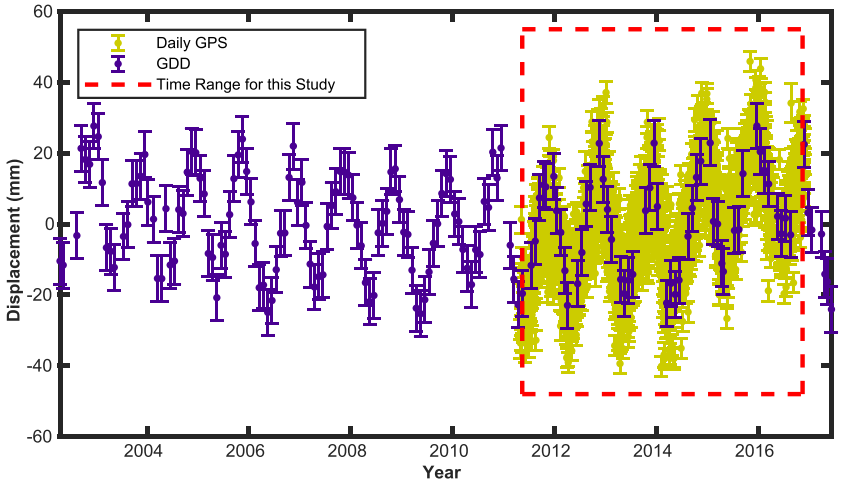

Figure 2. Displacement estimates in mm from daily GPS coordinate time series in yellow, overlain by monthly GRACE-derived displacement (GDD) estimates in blue for GPS station PAAT (see Figure 1). The PAAT time series begins almost 8 yr after the start of the GDD time series. The lengths of GPS time series vary from station to station, so we uniformly truncate both GPS and GDD time series to fit within the time span outlined by the red box.

3. Monthly Coordinate Time Series

3.1. GPS

To account for the inherently different sampling intervals of GPS and GRACE systems, we batched the daily GPS time series to form monthly averaged versions of the vertical coordinate time series data for each of the 23 GPS stations. Independent of sampling interval, time series of continuous GPS stations often contain phase center offsets associated with equipment changes, earthquakes, or other disturbances. If unaccounted for, unmodeled offsets would bias estimates for trend and seasonal motions or monthly averaged positions. Among the 23 stations in this study, the stations with the greatest number of offsets for the entire length of their time series are BRAZ and KOUR with 13 and 9 offsets, respectively. The rest of the stations have less than 3 offsets on average. Both SOPAC (http://sopac.ucsd.edu/) and NGL provide dates and descriptions of phase center offsets and earthquakes at the GPS stations in their databases. Using the offset epochs provided by the two institutions, we estimated offset magnitudes using the Hector software package (Bos et al., 2013), which uses the Maximum Likelihood Estimation method to estimate site motion model parameters (trend, seasonal motions, and phase center offsets), as well as model parameters describing noise processes. Of the 23 stations, 12 have offsets listed in the NGL database associated with distant earthquakes, such as the 2010 M8.8 Maule, Chile, earthquake or the 2014 M8.2 Iquique, Chile, earthquake. The closest earthquake epicenter with a cataloged offset was the 2015 M7.6 Iberia, Peru, earthquake, which was approximately 630 km away from station ROGM and 350 km away from station RIOB, but this earthquake occurred at a depth of 590 km (Hayes et al., 2017). All other earthquakes have epicenters over 1,000 km away from the stations.

Only 30.4% of the offsets appear to be statistically significant at the 95% confidence interval, (roughly 2σ). The largest statistically significant offsets, up to 67.2 $\pm$ 4.2 mm, are associated with equipment changes. Offsets associated with earthquakes are relatively small despite the rather large magnitudes of the earthquakes and are not statistically significant at the 95% confidence interval, as we might expect given the large distance between the GPS stations and the earthquakes.

We assume that postseismic deformation associated with these distant earthquakes is below the resolution of the GPS vertical coordinate time series data. If postseismic motions do contribute to the signal contained within the GPS time series data, we would expect them to manifest as biases in our estimates for secular rate, rather than biases in seasonal or other temporally variable motions.

We used the offset estimates to realign the time series segments before proceeding to form time series of monthly averages for more direct comparison with GDD time series. Then, we calculated the weighted

monthly average of the daily GPS vertical coordinate displacement data as

$$\bar{x}_{\text{month}} = \frac{\sum_{i=1}^{n} x_i \sigma_i^{-2}}{\sum_{i=1}^{n} \sigma_i^{-2}}, \tag{1}$$

where n is the number of (nominally daily) data points for the month, x_i is the ith vertical displacement, and σ_i is the uncertainty associated with the ith data point. GPS uncertainty is essentially a measure of the data precision determined during the raw GPS phase data processing. Estimates for the uncertainty associated with the monthly averages were calculated as

$$\sigma_{\bar{x}_{\text{month}}} = \hat{\sigma}\left(\sum_{i=1}^{n} \sigma_i^{-2}\right)^{-1/2}, \tag{2}$$

where σ_i is the uncertainty associated with the ith data point. The *a posteriori* scale factor $\hat{\sigma}$ was computed as

$$\hat{\sigma} = \left[\frac{1}{N-1}\sum_{i=1}^{N} r_i^2 \sigma_i^{-2}\right]^{1/2}, \tag{3}$$

where N is the number of data points and r_i is the ith residual between the observed data and corresponding monthly average. A more detailed explanation of this model (equation (6)) follows in section 4.

3.2. GRACE-Derived Displacements

In our analysis of GRACE data we closely follow the methods of Harig and Simons (2012), Harig and Simons (2015), and Harig and Simons (2016). The Level-2 CSR GRACE data products are released as Stokes coefficients to spherical harmonic functions, usually up to a bandwidth of degree and order $L = 60$. These functions are orthogonal when integrated over a sphere but lose their orthogonality over the partial sphere. As a result, a local spherical harmonic solution in a specific area of interest would require regularization while retaining all $(L+1)^2$ coefficients in the expansion. In order to create a local, accurate, and sparse representation of the gravity field, we transformed the spherical harmonic functions into a new basis of spherical Slepian functions (Simons & Dahlen, 2006). The spatiospectrally localized Slepian functions are a linear combination of spherical harmonic basis functions and are orthogonal over both a partial sphere and the whole sphere. The functions are designed such that they maximize their energy within the study region, in our case the Amazon basin, and minimize energy elsewhere on the globe. The region we have chosen is outlined in purple in Figure 1. The Slepian functions we produce are equivalent to spherical harmonics in that they cover up to degree $L = 60$, thus ensuring no loss of spatial resolution.

To obtain the Slepian basis for the Amazon, we first integrated the product of the spherical harmonics, Y_{lm} over our region R such that

$$\int_R Y_{lm} Y_{l'm'} \mathrm{d}\Omega = D_{lm,l'm'}. \tag{4}$$

The Slepian functions, g_{lm}, can then be obtained as eigenfunctions of the "localization kernel" $\mathbf{D}$ as

$$\sum_{l'=0}^{L} \sum_{m'=-l'}^{l'} D_{lm,l'm'} g_{l'm'} = \lambda g_{lm}. \tag{5}$$

The eigenvalues, λ, are a measure of the concentration of energy of each Slepian function in our region. The effective number of functions that are concentrated is given by the Shannon number, which is calculated as $M = (L+1)^2 A/(4\pi)$, where $A/(4\pi)$ is the area of the region of interest as a fraction of the globe. In truncating the basis at M, we concentrated signal in our area of interest. This greatly reduces the number of basis functions needed and allows for greater computational efficiency. The region we have chosen is the result of creating a convex hull around our GPS station locations and extending it outward by a 1° buffer.

For this region in the Amazon basin, $M = 36$ in comparison with the $(L+1)^2 = 3,721$ functions available before truncation.

We assume that the time variable gravity signals arise from variations in mass at Earth's surface, which deforms elastically to short-term mass loading. We express this deformation using Farrell's (degree-dependent) load Love numbers (Farrell, 1972; Wahr et al., 1998). The spherical harmonic coefficients, originally representing gravitational potential, were converted to surface displacement coefficients by multiplying them by their corresponding load Love number as

$$\hat{d}_{lm}^{\text{disp}} = a\frac{h_l'}{1+k_l'}\hat{d}_{lm}^{\text{pot}}, \tag{6}$$

where a is the Earth's radius, h_l' and k_l' are the degree-dependent load Love numbers, $\hat{d}_{lm}^{\text{pot}}$ is the gravitational potential data vector of spherical harmonic coefficients, and $\hat{d}_{lm}^{\text{disp}}$ is the surface displacement data vector of spherical harmonic coefficients. We used these deformation coefficients to evaluate the vertical displacements at the locations $\mathbf{r_i}$ of each of the 23 GPS stations for every month-year pair between March 2011 and November 2016.

Toward this end, we transformed the $\hat{d}_{lm}^{\text{disp}}$ data vector of spherical harmonic coefficients into coefficients of the truncated Slepian basis for each epoch in the monthly time series. We denote the transformed coefficients as $\hat{d}_\alpha(t_j)$. The displacement field of the Amazon basin is then simply a sum over the Slepian coefficients multiplied by the Slepian functions. We obtained

$$\hat{s}(\mathbf{r_i}, t_j) = \sum_{\alpha=1}^{M} \hat{d}_\alpha(t_j) g_\alpha(\mathbf{r_i}), \tag{7}$$

where $\hat{s}(\mathbf{r_i}, t_j)$ is the vertical component of the displacement of Earth's surface at location $\mathbf{r_i}$ and epoch t_j, $M = 36$ is the Shannon number and total number of functions used, $\hat{d}_\alpha(t_j)$ is the αth Slepian coefficient at epoch t_j, and $g_\alpha(\mathbf{r_i})$ is the αth Slepian function evaluated at $\mathbf{r_i}$.

To obtain the uncertainties associated with these estimates, we returned to the data vector of spherical harmonic coefficients for displacement $\hat{d}_{lm}^{\text{disp}}$. We used the time series of all 3,721 spherical harmonic coefficients in the GRACE epochs and performed a simple least squares fit of each spherical harmonic coefficient time series to a linear model supplemented by annual and semiannual terms. The residuals of these time series represent a conservative estimate of the noise, and their time-averaged variances were used to obtain the full covariance matrix $C_{lm,l'm'}$. We proceeded with the total covariance model, instead of only the diagonal elements, as Harig and Simons (2012) found that the off-diagonal terms significantly contributed to the observed spatial covariance.

We transformed the spherical harmonic covariance matrix into our Slepian basis as

$$C_{\alpha,\beta} = g_{lm,\alpha}\ C_{lm,l'm'}\ g_{l'm',\beta}, \tag{8}$$

where $C_{\alpha,\beta}$ is the covariance matrix in the Slepian basis and $g_{l'm',\beta}$ is the transpose of $g_{lm,\alpha}$, the matrix of eigenfunctions (equation (5)). An estimate of surface displacement uncertainty for a GPS station location at $\mathbf{r_i}$ was then calculated as

$$\sigma^2(\mathbf{r_i}) = \sum_{\alpha=1}^{M}\sum_{\beta=1}^{M} g_\alpha(\mathbf{r_i})\ C_{\alpha,\beta}\ g_\beta(\mathbf{r_i}). \tag{9}$$

GRACE mascons are also a popular alternative to using spherical harmonic coefficients alone, as they are accessible and useful to people of all experience levels (Watkins et al., 2015). Mascon solutions can provide highly accurate estimates of mass loading, as they implement a smoothing process via regularization, rather than applying a filter to the postprocessed data. Mascons are also useful as they (e.g., JPL solutions) can resolve a mass loading signal over gridded cells that are as small as 1° by 1°. The accuracy of these 1° by 1° gridded solutions is further improved by multiplying them by a scaling grid, which is computed using a land-hydrologic model (Landerer & Swenson, 2012).

Alternatively, Slepian functions do not require smoothing or scaling processes, which simplifies analyses using GRACE data. The mascons are also prone to leakage when using mascon blocks that include both

ocean and land signals, which may be improved using a Coastline Resolution Improvement filter (Wiese et al., 2016). The Slepian functions further reduce the need for filtering as they are inherently designed to minimize leakage from the chosen region of interest. Slepian functions, similar to mascons, provide a significant reduction in the ratio of signal-to-noise. However, the Slepian functions have an additional advantage because data are concentrated in the sparse Slepian basis, and, as a result, relatively few basis functions are required. Depending on the resolution of the mascon solution, there may be an order of magnitude more mascon blocks than Slepian functions required to visualize the data within the same region of interest.

3.3. GPS-GDD

Computation of the GPS-GDD time series was performed by simple subtraction. In the process of subtracting one time series from another, only the epochs that overlap between GPS and GDD are included. The uncertainties associated with the residuals are calculated as

$$\sigma_{\text{GPS-GDD}} = (\sigma^2_{\text{GPS}} + \sigma^2_{\text{GDD}})^{1/2}, \tag{10}$$

which assumes that the GPS and GDD errors are uncorrelated with one another.

4. Analysis of Vertical Displacement Time Series

We used the program Hector (Bos et al., 2013) to fit the monthly GPS, GDD, and GPS-GDD time series data using a traditional kinematic model of the form

$$d_i = w \cdot \mathrm{d}t_i + z + A \cdot \sin(f_a \mathrm{d}t_i) + B \cdot \cos(f_a \mathrm{d}t_i) + C \cdot \sin(f_s \mathrm{d}t_i) + D \cdot \cos(f_s \mathrm{d}t_i) + e_i, \tag{11}$$

where d_i is the ith monthly observation for a station, w is the vertical rate, $\mathrm{d}t_i$ is the time passed since the reference epoch, z is the offset at the reference epoch, A and B are coefficients scaling the sine and cosine components of annual amplitude, C and D are coefficients scaling the sine and cosine components of semiannual amplitude, and f_a and f_s are the annual and semiannual frequencies, respectively. Hector uses the Maximum Likelihood Estimation method to estimate these model parameters and their respective uncertainties, along with the parameters of a noise model representing the error process e_i. We assumed that the error process is well described by a Generalized Gauss Markov (GGM) noise model. A GGM is a Gauss Markov noise model with an additional parameter κ (Langbein, 2004), approximating correlated noise at low frequencies and flattening to white noise at high frequencies.

When we refer to high frequencies in this analysis, we are referring to the frequencies (usually larger than 1 cpy) at which the power spectra flatten to a constant value. This value represents the variance of the white noise component of the error spectrum. Low frequencies are the generally less than 1 cpy. At these low frequencies, the error spectrum behavior reflects time correlation in the residuals, which may derive from time-correlated errors or from unmodeled signals. We measure this behavior using the κ value or the slope of the error spectrum at low frequencies.

Specifically, the value of κ characterizes noise type, with $\kappa = -2$ indicating the presence of a dominant random walk process, $\kappa = -1$ indicating the presence of a dominant flicker noise process, and $\kappa = 0$ representing white (uncorrelated) noise (Williams, 2003). Spectral indices with noninteger values in the range $-2 < \kappa < -1$, that is , between random walk and flicker noise, are associated with the family of noise processes referred to as fractional Brownian motion. Spectral indexes in the range $-1 < \kappa < 0$ are associated with the family of noise processes referred to as fractional Gaussian noise (Mandelbrot & Van Ness, 1968).

To ensure that the spectral characteristics of the time series data are sufficiently well-resolved, we analyzed the data in two ways. First, we made the simplifying assumption that the noise process in the GPS time series affects all stations equally, despite variation in station equipment or location. We also assumed that the noise in the GDD time series is independent of location. With these assumptions, we obtained model residuals for all 23 GPS time series and concatenated them to generate time series of GPS, GRACE, and GPS-GDD residuals that contain nominally 69 monthly values. We generated 1,000 of these concatenated time series for the GPS, GDD, and GPS-GDD residuals, each with a different random ordering of stations. We found that κ varied only slightly between the randomly ordered, concatenated GPS residual time series, with a standard deviation of about 0.02. The weighted average κ for these 1,000 concatenated GPS residuals is -1.2759 ± 0.0007. Hector also outputs a weighted average κ value of -0.6133 ± 0.0006 for GDD and

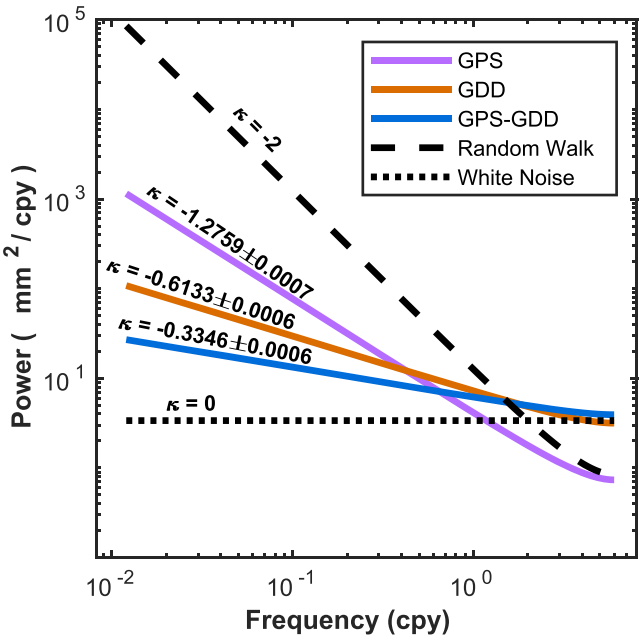

Figure 3. Power spectrum plots for the κ value of GPS, GDD, and GPS-GDD concatenated residual time series, plus two reference lines. The κ values are the weighted average of 1,000 concatenated residual time series, each with with a different order of stations. The solid reference line is created using a κ value of −2, representing random walk at low frequency, and the dotted line is created using a κ value of 0, representing white noise.

−0.3346±0.0006 for GPS-GDD. Similarly, the variation between the 1,000 randomly concatenated time series for the GDD and GPS-GDD residuals is small, with a standard deviation of about 0.02 and 0.02, respectively.

We also computed κ values for each station location independently, then formed an average among locations (Figure S5 and Table S1). We have found that the average κ among these individual stations for GDD (−0.65 ± 0.08) and GPS-GDD (−0.34 ± 0.08) are the same (to within their uncertainties) as the κ values that resulted from this concatenated residuals analysis. The averaged κ for the individual GPS stations (−1.49 ± 0.04) is slightly larger than the concatenated time series κ. Both estimates suggest that the GPS error spectrum is in the fractional Brownian regime. We choose to focus our discussion on the results of the concatenated analysis shown in Figure 3 because the formal uncertainties are two orders of magnitude lower. The conclusion we derive from this analysis is independent of which estimate we use.

To test whether GPS and GDD compare well over longer time scales, we performed a second analysis using the longest running GPS stations. We fit the line from equation (11) to the complete GPS time series for stations BELE, BRAZ, CUIB, and KOUR. The latter three have the longest time series, with GPS observations extending back to the onset of the GRACE observations (April 2002). Station BELE only has observations extending back to January 2004. We computed GDD and GPS-GDD for these station locations over the full duration of the GPS time series. These longer time series are plotted in Figures S1–S4. Their corresponding estimates for vertical rate, annual amplitude, semiannual amplitude, and κ are provided alongside each plot.

The weighted average κ for the four, full time period, GPS time series is −1.20 ± 0.13, marginally smaller than the weighted average κ obtained for the shorter time series but still in the fractional Brownian motion regime. Similarly, the weighted average κ for the four full GDD time series (−0.37 ± 0.03) is slightly lower than the weighted average κ we obtained from the shorter time series. These slightly smaller values may reflect a more accurate determination of low-frequency noise afforded by the longer time series. Importantly, the weighted average κ we obtain from an analysis of GPS-GDD, −0.52 ± 0.03, is significantly lower than that for GPS alone, showing that the result also holds for the full time series.

To further assess the fit of the kinematic model to time series data, we computed the weighted root-mean-square (WRMS) misfit for each station for the GPS, GDD, and GPS-GDD data sets. WRMS is a measure of the precision of the measurements relative to the kinematic model and has units of the

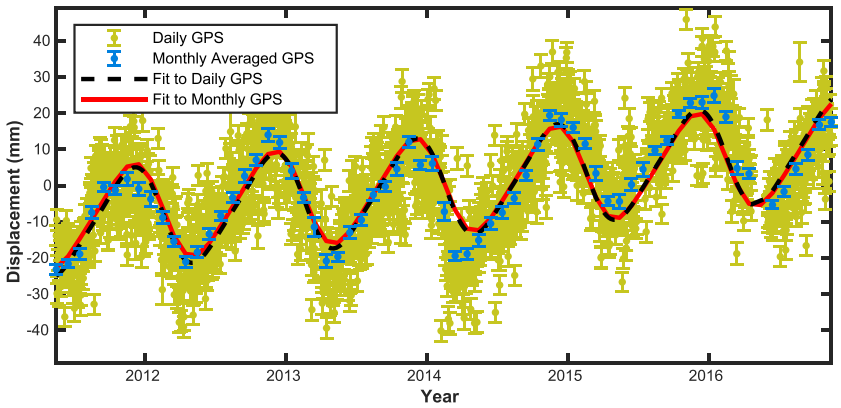

Figure 4. Observed and modeled GPS time series at station PAAT for (1) daily observed GPS time series in yellow points with error bars, (2) best fit model to the daily GPS time series as a dashed black line, (3) monthly averaged GPS time series in blue points with error bars, and (4) best fit model to the monthly averaged GPS time series as a solid red line. The time period is truncated to the window outlined in Figure 2. The best fit lines are of the form shown in equation (11).

measurement type (in our case, displacement) and is calculated as

$$\mathrm{WRMS} = \left[\frac{\frac{N}{N-1} \sum_{i=1}^{N} \frac{(\hat{s}_i - d_i)^2}{\sigma_i^2}}{\sum_{i=1}^{N} \frac{1}{\sigma_i^2}} \right]^{1/2}. \tag{12}$$

Here, N is the number of monthly observations at each station, $\hat{s}_i$ is the modeled displacement signal, d_i is a month's observation, and σ_i is the uncertainty of each data point. The WRMS statistic is commonly used as a measure of repeatability of measurements but does not account for the temporal correlation among the errors, as shown in Figure 3. Thus, its value depends on the duration of the time series. It is nevertheless useful for intercomparisons among stations with time series of roughly equal length.

The parameter uncertainties determined using Hector depend on the fit of the kinematic model to the data. If the time series data exhibit near-perfect secular and periodic motions with uncorrelated (white) errors, the traditional kinematic model should adequately represent the signal, and the resulting noise model would indicate little frequency dependence ($\kappa \sim 0$). However, if site motion is not well represented by the traditional kinematic model, the resulting noise model will likely exhibit a stronger temporal correlation ($-2 \leq \kappa < 0$), even if the observational error process is temporally uncorrelated (e.g., Bennett, 2008; Bogusz & Klos, 2016; Van Camp et al., 2010).

4.1. Model Fit to GPS

Before proceeding with our analysis of the monthly averaged GPS coordinate time series, we first confirmed that the model fit to the monthly time series is statistically indistinguishable from the original daily time series to within uncertainties (Figure 4). The correlation coefficient is 0.99 between daily-derived and monthly-derived vertical rate, 1.00 between daily-derived and monthly-derived annual amplitudes, and 0.99 between daily-derived and monthly-derived semiannual amplitudes. The close agreement validates our treatment of time series offsets before forming monthly averages.

Values that provide a measure of misfit of the kinematic model to the monthly averaged coordinate time series data are provided in Table 1. The parameter estimates that give the best fit to the time series data are listed in Table 2. The WRMS values for GPS range between 2.72 and 8.62 mm, with an average value of 4.23 mm. We note that there is a high degree of spatial variation in GPS rate and amplitude estimates and their uncertainties. Station-to-station variations in GPS parameter estimate uncertainties could result from issues with station performance (e.g., multipath, sky obstructions, and data gaps) or could indicate the presence of a displacement signal that is not well represented by the traditional kinematic model. We note that

Table 1
Table of Values Associated With the GPS, GDD, and GPS-GDD (Here Represented as "GMG") Coordinate Time Series in Our Study

	Num. epochs			Avg. pos. σ (mm)			WRMS (mm)		
SID	GPS	GDD	GMG	GPS	GDD	GMG	GPS	GDD	GMG
BELE	67	50	50	1.35	5.53	5.69	3.90	5.22	6.55
BOAV	67	50	50	1.21	6.06	6.19	5.04	5.86	7.91
BRAZ	65	50	48	1.10	4.34	4.50	2.72	3.66	7.30
CUIB	67	50	50	1.20	4.03	4.22	3.21	4.57	5.83
KOUG	65	50	49	1.43	5.39	5.61	2.81	5.20	5.47
KOUR	58	50	42	1.43	5.33	5.55	3.23	5.02	5.70
MAPA	66	50	49	1.45	5.30	5.51	3.37	4.33	6.44
MTCN	64	50	48	1.19	6.19	6.31	3.48	4.93	6.81
MTCO	67	50	50	1.16	6.08	6.20	4.50	7.13	6.57
MTSF	66	50	49	1.21	6.06	6.19	3.32	5.62	5.61
MTSR	67	50	50	1.24	5.86	6.01	5.22	6.86	6.17
NAUS	63	50	47	1.38	8.31	8.43	8.62	9.59	8.58
PAAT	66	50	49	1.55	6.48	6.67	4.56	5.82	6.17
PAIT	59	50	43	1.41	7.91	8.04	7.79	7.38	8.86
PMB1	67	50	50	1.46	4.37	4.62	3.14	3.27	6.80
POVE	67	50	50	1.24	6.53	6.65	3.37	7.58	10.16
RIOB	67	50	50	1.31	6.66	6.80	2.99	6.17	10.35
ROCD	67	50	50	1.27	5.40	5.54	4.77	4.84	5.96
ROGM	66	50	50	1.30	5.79	5.94	4.28	7.65	8.13
ROJI	67	50	50	1.25	5.60	5.75	4.13	6.21	8.78
SAGA	67	50	50	1.62	6.42	6.62	4.98	5.74	9.37
SRZN	63	50	46	1.50	4.93	5.17	4.12	3.70	5.05
TOGU	67	50	49	1.15	6.24	6.36	3.83	5.99	5.36
Average	65.4	50.0	48.7	1.32	5.86	6.03	4.23	5.76	7.13

Note. Columns include the number of epochs in each time series, the average position uncertainty, and the WRMS values.

there are few gaps in the data, as well as relatively uniform day-to-day and station-to-station coordinate time series displacement uncertainties. It is also notable that station-to-station variation among monthly averaged $\sigma_{\bar{x}_{\text{month}}}$ values is reasonably low. This indicates that whatever process is responsible for variability in parameter estimate uncertainty and WRMS is not associated with station-to-station variation in daily position precision determined during the raw GPS phase data processing or gaps in the data. These observations suggest that the station-to-station variation in parameter estimate uncertainties instead results from differing amounts of model misfit being mapped into the GGM noise model. This interpretation is supported by the high correlation between WRMS values and parameter estimate uncertainties. The correlation coefficient is 0.96 between WRMS and vertical rate uncertainties, 0.94 between WRMS and annual amplitude uncertainties, and 0.76 between WRMS and semiannual amplitude uncertainties. Further, data gaps would naturally result in larger parameter estimate uncertainties, but they would not necessarily result in higher WRMS values, since all coordinate time series data points are nearly equally precise.

The κ value estimated for GPS from the concatenation analysis is -1.2759 ± 0.0007, suggesting that, on average, GPS exhibits noise in the fractional Brownian motion regime (Figure 3). Upon investigating the individual station κ values (Table S1), we find that NAUS and PAIT, the stations with the highest WRMS values, have κ values representing the greatest correlation in the low-frequency noise (κ estimate of -1.71 ± 0.02 for NAUS and -1.56 ± 0.01 for PAIT). This further supports our inference that station-to-station variation in parameter estimate uncertainty is a symptom of model misfit being mapped into the GGM noise model, rather than reflecting variable station performance.

Table 2
Table of Parameters Used in the Model for the GPS, GDD, and GPS-GDD (Here Represented as "GMG") Coordinate Time Series in Our Study

	Vert. rate. (mm/yr)			Ann. amp. (mm)			Semiann. amp (mm)		
SID	GPS	GDD	GMG	GPS	GDD	GMG	GPS	GDD	GMG
BELE	2.92 ± 0.87	1.64 ± 0.58	1.39 ± 0.58	7.66 ± 0.63	7.08 ± 1.08	1.57 ± 0.81	2.05 ± 0.43	1.63 ± 0.81	3.39 ± 1.08
BOAV	5.18 ± 1.45	2.78 ± 0.43	3.08 ± 0.29	10.29 ± 0.91	8.34 ± 1.10	3.84 ± 0.84	2.03 ± 0.59	1.49 ± 0.78	1.66 ± 0.80
BRAZ	−1.88 ± 0.70	1.63 ± 0.28	−3.48 ± 0.48	9.26 ± 0.60	6.43 ± 0.70	2.85 ± 0.88	1.67 ± 0.42	1.44 ± 0.63	1.32 ± 0.66
CUIB	2.51 ± 0.66	1.03 ± 0.74	1.82 ± 0.48	9.08 ± 0.61	11.91 ± 0.91	3.00 ± 0.87	1.10 ± 0.42	2.26 ± 0.73	1.72 ± 0.75
KOUG	2.32 ± 0.39	1.49 ± 0.45	0.65 ± 0.35	6.01 ± 0.57	6.66 ± 1.02	3.20 ± 0.89	2.35 ± 0.49	2.33 ± 0.94	1.36 ± 0.70
KOUR	−0.46 ± 0.64	1.53 ± 0.45	−1.94 ± 0.31	5.88 ± 0.70	6.32 ± 0.99	2.84 ± 0.79	2.15 ± 0.53	2.20 ± 0.90	1.18 ± 0.62
MAPA	2.75 ± 0.58	1.33 ± 0.38	1.34 ± 0.21	7.78 ± 0.66	12.77 ± 0.86	6.90 ± 0.62	1.49 ± 0.50	2.36 ± 0.82	1.59 ± 0.64
MTCN	3.26 ± 0.67	1.26 ± 0.26	2.33 ± 0.35	8.71 ± 0.64	12.04 ± 0.77	3.75 ± 0.90	1.78 ± 0.47	2.54 ± 0.83	1.77 ± 0.83
MTCO	3.45 ± 1.04	3.30 ± 1.43	0.83 ± 0.88	12.60 ± 0.69	15.07 ± 1.34	3.01 ± 1.15	1.38 ± 0.44	2.02 ± 0.91	1.66 ± 0.83
MTSF	3.25 ± 0.82	2.32 ± 0.74	1.11 ± 0.37	13.34 ± 0.69	12.19 ± 1.18	2.15 ± 0.86	1.74 ± 0.48	1.39 ± 0.73	1.86 ± 0.84
MTSR	1.08 ± 1.46	2.72 ± 1.31	−0.93 ± 0.97	13.74 ± 0.80	13.95 ± 1.29	2.55 ± 1.10	1.26 ± 0.47	1.97 ± 0.89	2.27 ± 0.95
NAUS	−1.58 ± 4.08	1.67 ± 2.11	−1.69 ± 1.18	29.62 ± 1.44	26.76 ± 1.80	3.04 ± 1.35	4.26 ± 0.83	2.89 ± 1.22	3.14 ± 1.23
PAAT	3.45 ± 1.32	2.43 ± 1.00	1.67 ± 0.41	13.23 ± 0.81	16.94 ± 1.20	3.69 ± 0.95	1.95 ± 0.52	2.38 ± 0.93	1.50 ± 0.76
PAIT	0.17 ± 3.38	4.33 ± 1.38	−2.75 ± 1.24	14.89 ± 1.51	18.73 ± 1.43	4.88 ± 1.62	1.31 ± 0.68	1.44 ± 0.75	2.18 ± 1.10
PMB1	−1.74 ± 0.58	1.63 ± 0.27	−3.10 ± 0.33	5.69 ± 0.65	5.21 ± 0.64	1.10 ± 0.57	2.59 ± 0.51	0.91 ± 0.47	2.92 ± 0.77
POVE	−3.33 ± 0.84	0.94 ± 1.25	−4.19 ± 1.30	14.81 ± 0.67	15.46 ± 1.52	2.94 ± 1.35	1.76 ± 0.46	1.77 ± 0.92	2.78 ± 1.19
RIOB	−3.74 ± 0.35	0.22 ± 0.62	−3.98 ± 0.83	10.33 ± 0.58	12.16 ± 1.26	4.15 ± 1.48	2.24 ± 0.50	2.02 ± 0.99	2.29 ± 1.15
ROCD	0.29 ± 1.11	−0.62 ± 0.45	1.48 ± 0.59	12.82 ± 0.77	12.04 ± 0.97	2.22 ± 0.96	1.45 ± 0.50	2.69 ± 0.92	2.49 ± 0.94
ROGM	−0.58 ± 0.93	0.41 ± 1.43	−0.98 ± 1.36	14.93 ± 0.96	14.01 ± 1.52	2.35 ± 1.20	1.87 ± 0.69	1.95 ± 0.97	2.98 ± 1.23
ROJI	2.76 ± 1.42	0.19 ± 1.09	3.11 ± 0.54	12.43 ± 0.70	17.55 ± 1.26	5.76 ± 1.12	1.64 ± 0.43	2.13 ± 0.92	2.65 ± 1.03
SAGA	−2.69 ± 1.51	1.49 ± 0.74	−4.03 ± 0.62	11.49 ± 1.01	9.00 ± 1.21	5.49 ± 1.11	1.01 ± 0.51	1.53 ± 0.79	1.52 ± 0.78
SRZN	2.74 ± 0.52	1.89 ± 0.32	0.62 ± 0.40	6.46 ± 0.68	6.27 ± 0.73	2.44 ± 0.87	2.20 ± 0.55	0.97 ± 0.51	2.17 ± 0.86
TOGU	4.38 ± 1.02	3.62 ± 0.82	1.16 ± 0.26	10.70 ± 0.69	12.00 ± 1.25	2.48 ± 0.72	1.18 ± 0.44	2.26 ± 0.99	1.91 ± 0.76
Average	0.51 ± 0.59	1.52 ± 0.16	0.55 ± 0.43	10.18 ± 0.76	10.29 ± 0.92	3.21 ± 0.34	1.75 ± 0.11	1.72 ± 0.12	1.90 ± 0.12

Note. Columns include vertical rates, annual amplitudes, and semiannual amplitudes. All reported average values were calculated with a weighted least squares averaging method.

4.2. Model Fit to GDD

The best fit to the GDD time series results in WRMS residuals in the range of 3.27 to 9.59 mm with an average WRMS value of 5.76 mm (Table 1). The spatial variation in vertical rates and amplitudes obtained from the GDD time series data is less evident than in GPS observations. This is possibly because GRACE resolves largely long-wavelength deformation, thus ensuring some uniformity of the signal between nearby locations. The κ estimate for GDD is -0.6133 ± 0.0006 (Figure 3), which is in the fractional Gaussian regime, and indicates that the GDD time series contain some signal not well represented by the applied kinematic model or that the time series contain some amount of time-correlated measurement error (Figure 3). Despite a smaller station-to-station variation relative to the GPS time series analysis results presented above in section 4.1, the rate and amplitude uncertainties for GDD are also correlated with their WRMS values. For the GDD time series, the correlation coefficient is 0.93 between WRMS and vertical rate uncertainties, 0.98 between WRMS and annual amplitude uncertainties, and 0.76 between WRMS and semiannual amplitude uncertainties. Looking to individual stations, NAUS and PAIT again have the greatest parameter uncertainties, higher WRMS values, and κ values indicating a high degree of correlation in the noise.

We also observe a moderate correlation between GPS and GDD WRMS values, as illustrated in Figure 5, where the r^2 value is 0.46. This slight correlation suggests that some of the inferred error associated with both the GPS and GDD time series may be associated with a common process. We will test this hypothesis in subsequent sections.

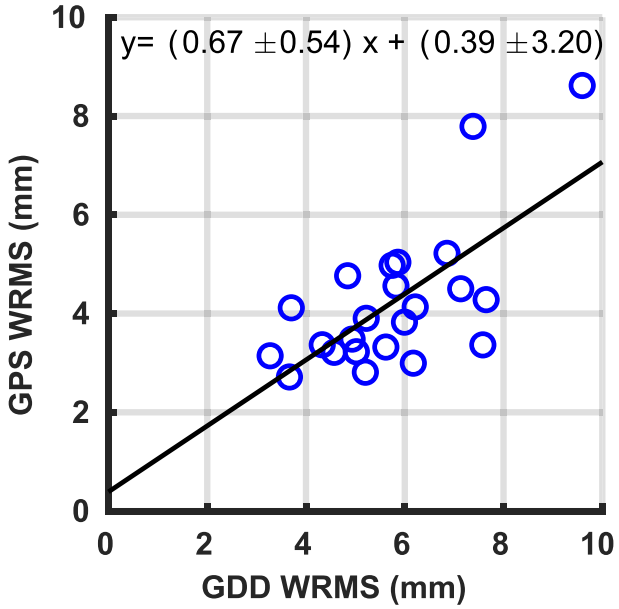

Figure 5. A scatter plot showing the relationship between the WRMS values of GDD and GPS. The r^2 for the best fit line is 0.46.

4.3. GPS-GDD and Model Fit

To explore the extent to which GPS vertical time series record the mass loading signal in the Amazon, we analyze the GPS-GDD time series following the same procedure as for the GPS and GDD time series presented above. Here we assume that GPS and GDD error processes are uncorrelated with one another. We further assume that any non-mass loading signal that is recorded by GPS, but not GDD, is also uncorrelated with the GDD error process and thus would be relatively unaffected by differencing. However, if both time series contain a common signal, even if it is not well represented by the kinematic model, it should be reduced in the GPS-GDD time series.

With these assumptions, we may assess the error spectrum of the GPS-GDD residuals at high frequencies. From Figure 3, the white noise in the GPS error spectrum is about 0.7 mm^2/cpy, which is much lower than the approximately 3.2 mm^2/cpy white noise observed for the GDD displacement time series. Not surprisingly, the variance of the white noise in the GPS-GDD residuals (about 3.9 mm^2/cpy) is slightly larger than that of the GDD spectrum, consistent with the GPS and GDD error processes being statistically independent of one another.

Separately, we asses the error spectrum of the GPS-GDD residuals at low frequencies. We see that the κ value estimate for the GPS-GDD analysis is -0.3346 ± 0.0006, significantly smaller than the spectral index inferred from GPS alone. Like the κ estimate arising from our analysis of the GDD time series, this value of κ for GPS-GDD is in the fractional Gaussian regime, though with a slope that is somewhat closer to white noise. Our analysis of the error spectra provided in Figure 3 strongly suggests that both systems record similar mass loading signals, which are not completely represented using a kinematic model consisting of a secular trend and perfectly periodic seasonal variations only.

In contrast to the GDD and GPS results also presented in Table 1, the WRMS values for GPS-GDD do not correlate as strongly with the parameter estimate uncertainties. The correlation coefficient is 0.62 between WRMS and vertical rate uncertainties, 0.73 between WRMS and annual amplitude uncertainties, and 0.63 between WRMS and semiannual amplitude uncertainties. Looking to NAUS and PAIT once more, we see that they still have the highest average position uncertainties of all 23 stations. But their WRMS values are no longer strongly correlated with their position uncertainties.

4.4. Secular Vertical Rates of Displacement

Given that all 23 GPS stations are situated on the South American craton, over 1,000 km from the Nazca and Caribbean plate boundaries, we do not expect appreciable steady-state contribution to vertical motion captured by the GPS coordinate time series arising from tectonic strain accumulation. Moreover, given the large

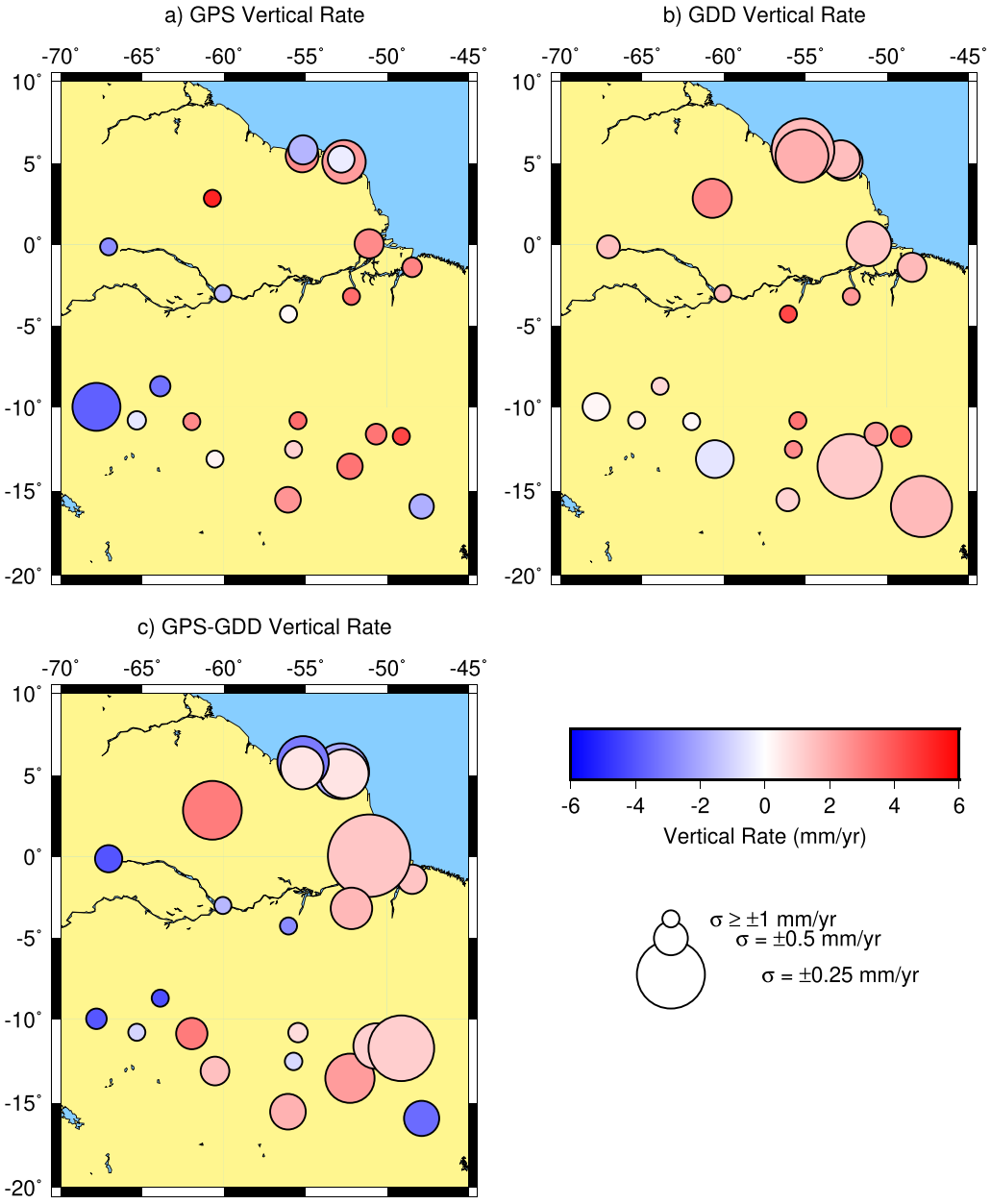

Figure 6. Spatial distribution across the Amazon basin of vertical rates (mm/yr) for (a) GPS, (b) GDD, and (c), GPS-GDD. Each circle is plotted at its associated GPS station location. Circle colors indicate the magnitude of the rate. The size of the circles is inversely proportional to the uncertainties associated with the estimate; larger circles indicate smaller uncertainties.

hypocentral distances to all recent large magnitude earthquakes, we expect ongoing postseismic contributions to the vertical motion observed by GPS to also be minimal. Thus, in the absence of secular changes in mass loading, we would expect an estimated vertical rate near zero on average. Figure 6a shows the vertical rate (in mm/yr) and uncertainties for all 23 continuous GPS stations in our analysis across the Amazon basin.

Figure 6a shows that there is substantial variation in the magnitude of the GPS vertical rates, with some stations differing almost 9 mm/yr from other stations. The vertical rates for GDD (Figure 6b) exhibit less spatial variation than GPS, with the spread of values of nearly 5 mm/yr between the lowest and highest values. The basin-wide weighted average vertical rate is 0.51 ± 0.59 mm/yr for GPS and 1.52 ± 0.16 mm/yr for

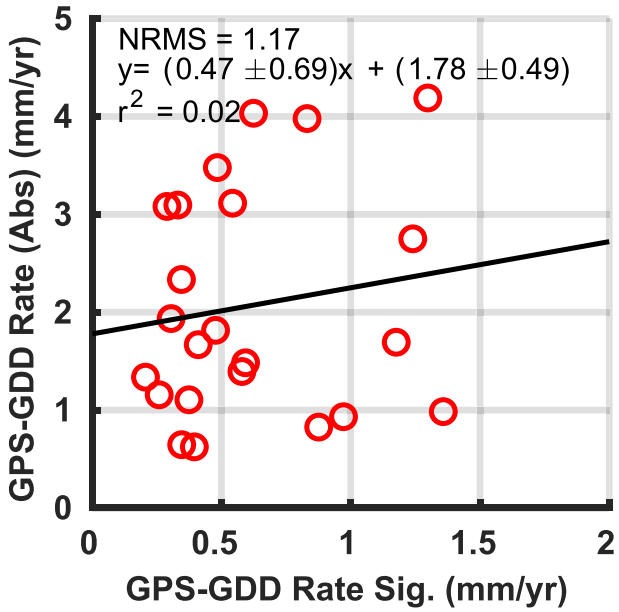

Figure 7. Scatter plot where GPS-GDD rates are plotted as a function of their corresponding uncertainties. A best fit line is plotted, along with its equation, the r^2 value, and the NRMS value.

GDD. These values differ at greater than the 99.9% confidence level, although both data sets are consistent with a small, secular uplift. The weighted average of GPS and GDD secular rates is 1.20 ± 0.26 mm/yr.

In our attempt to identify the source of disagreements between GPS and GDD, we note that there are four GPS stations in the northernmost portion of the study region (KOUR and KOUG and PMB1 and SRZN; Figure 1) that exhibit high variability among rate estimates within a distance of only 30 to 50 km, respectively (Figure 6a). The difference between KOUR and KOUG station pairs is 2.78 ± 0.75 mm/yr, and the difference between station pairs PMB1 and SRZN is 4.47 ± 0.78 mm/yr. These statistically significant disagreements between relatively nearby stations are a strong indication that a significant fraction of the rate variation observed in the GPS data, and thus variation in the GPS-GDD differences, might be associated in with errors in GPS vertical rate estimates.

The observed pattern in the GPS and GDD maps of Figure 6 is not consistent with postseismic deformation associated with recent large magnitude earthquakes or tectonic strain accumulation. In the case that the subduction zone was significantly contributing to this pattern, we should expect any subsidence signal to be at or nearest to the trench, with the strongest uplift signals also occurring close to the trench. For reference, this subduction zone is visible in the subsetted map in Figure 1 as the plate boundary that hugs the west coast of northern South America. Numerical models (e.g., Kanda & Simons, 2010) show positive vertical velocities decreasing substantially with distance inboard from the trench, going near to zero at only 10 times the locking depth of the subduction zone. This supports our expectation that such signals are small at the large distance of our study from the plate boundary to the west.

Looking at Figure 6c, the difference between rate estimates also exhibits a varying spatial pattern, with negative vertical rates in the westernmost stations, as well as at stations PAIT and NAUS near the Amazon River, the southernmost station BRAZ, and stations PMB1 and KOUR. All other stations have relatively small positive residual trends, except for stations ROJI and BOAV, which have the largest positive rates of all GPS-GDD time series, and are also located on the western side of our study area.

In examining Figure 6c, the reader may wonder whether the magnitude of GPS-GDD correlates with rate uncertainty. However, Figure 7 demonstrates that there is only a weak correlation of these rate magnitudes and uncertainties. One possibility for this is that the differences arise from short-wavelength components of the mass loading field that affect GPS but are below the resolution of GRACE. Another possibility is that the uncertainties in the rate differences underestimate the true uncertainties, such that none of the differences are statistically different from zero, relative to the true error model.

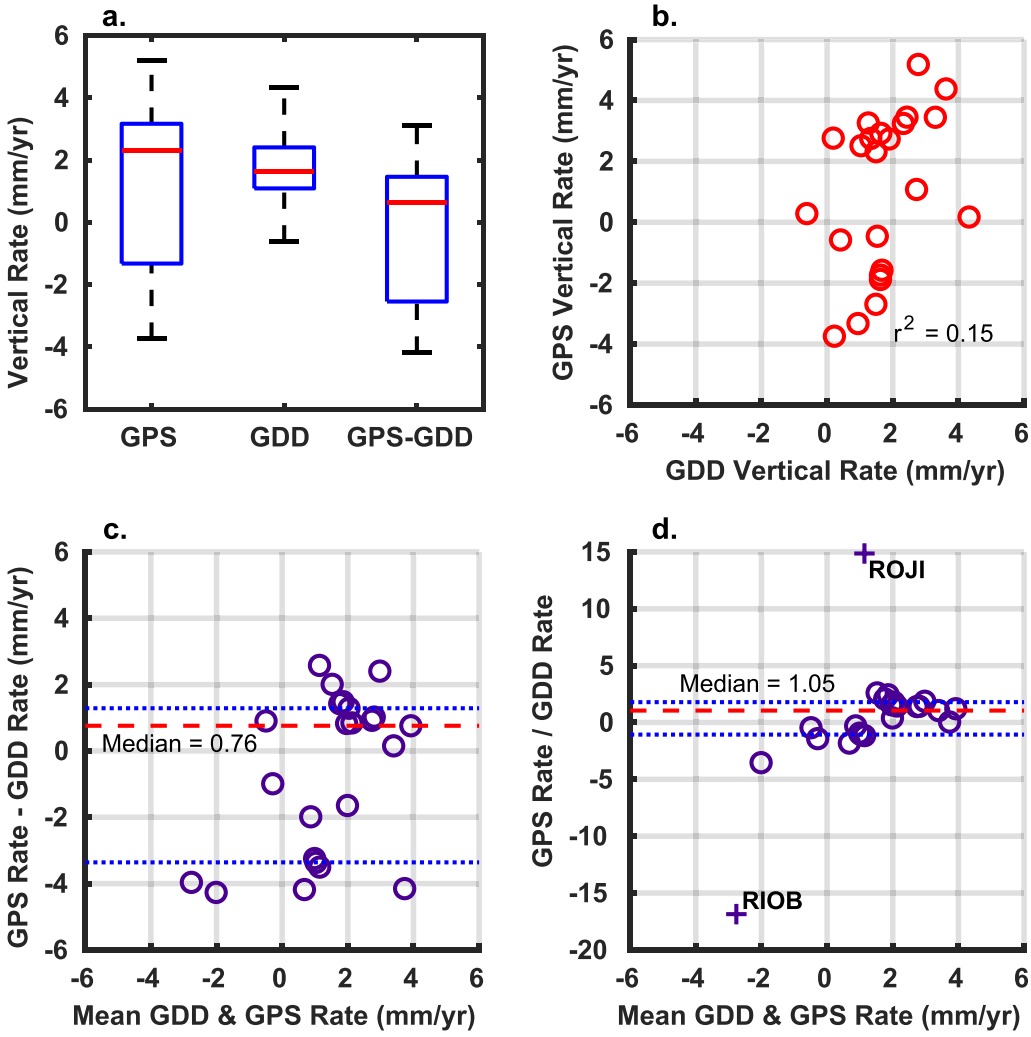

Figure 8. (a) Three boxplots of the vertical rates found using the time series of (1) GPS, (2) GRACE-derived displacement, and (3) GPS-GDD residuals at the 23 GPS site locations. The red line represents the median of the vertical rates; the blue box surrounds the interquartile range. It is important to note that the boxplot for GPS-GDD residuals is made using the rate estimated from the actual GPS-GDD time series and not from the set of GPS rates-GDD rates. (b) A scatter plot comparing GPS vertical rates with GDD vertical rates at all 23 GPS stations. The r^2 between the data is 0.15. (c) Bland-Altman plot with the mean of GPS and GDD vertical rates on the x axis and difference between them on the y axis. The dashed red horizontal line represents the median of the differences. (d) Bland-Altman plot with mean of GPS and GDD vertical rates on the x axis and ratio of the rates (GPS/GDD) on the y axis. The dotted lines and dashed lines represent the quartiles and the median. The purple plus signs represent the outliers, ROJI and RIOB. Outliers are found by identifying data points that are 3 interquartile ranges below the first quartile or 3 interquartile ranges above the third quartile.

Figure 8 provides a comprehensive diagrammatic representation of the vertical rate estimates from GPS and GDD. In Figure 8a, we represent the data using boxplots, which visually represent the data without making any assumptions about the underlying statistical distribution. We can measure the dispersion of the data by comparing the total range of values with the interquartile range (IQR) which is obtained from subtracting the third quartile (the median of the upper half of the data) from the first quartile (the median of the lower half of the data). The black "whiskers" indicate the maximum and minimum of all vertical rates for each data type and enclose the total range. The medians of GPS (2.32 mm/yr) and GDD (1.63 mm/yr) are similar to one another and slightly closer than the weighted means discussed above. As with the weighted means, both medians are positive. There is greater variation among GPS rate estimates (total range = 8.93 mm/yr, IQR = 4.49 mm/yr) than in GDD (total range = 4.94 mm/yr, IQR = 1.32 mm/yr). Subtraction of GDD from GPS time series results in a median vertical rate that is closer to zero (0.65 mm/yr) and a slightly reduced variation

in rates (total range = 7.30 mm/yr, IQR = 4.01 mm/yr) relative to the collection of GPS rate estimates. The GPS-GDD boxplot (Figure 8a) shows that subtracting GDD from GPS reduced the median vertical rate by about 72%, the range by ~18%, and the IQR by ~11%.

We plot the rates estimated from GPS and GDD against each other in the scatter plot in Figure 8b. There is virtually no correlation among the data, with an r^2 of 0.15. The absence of a correlation is worth investigating further. We thus continue to assess the relationship between GPS and GDD rates in Figures 8c and 8d.

An alternative method of gauging the agreement between two variables is the Bland-Altman plot, a tool that is commonly used to evaluate the agreement among two different measurement techniques (Bland & Altman, 1986). Figures 8c and 8d are Bland-Altman plots where the difference between GPS and GDD rates at each station (Figure 8c) or the ratio of GPS to GDD (Figure 8d) is plotted as a function of the combined GPS and GDD mean values. Bland-Altman plots are designed to identify bias and scale differences among parameter estimates deriving from different measurement systems and can be thought of as a way to gauge agreement rather than correlation. A typical Bland-Altman plot also displays a horizontal line at the mean of the differenced data and horizontal lines for the 95% confidence region spanning the range between 1.96 and −1.96 standard deviations from the mean. The Bland-Altman plots in Figure 8 are different in that we plot the first and third IQRs instead of the standard deviations and the median of the data instead of the mean. These measures are independent of the (unknown) error distribution, which make them ideal for analyzing variations in the absence of knowledge of the underlying error processes (Tukey, 1977).

To the extent that GPS and GDD rate data are similar, we expect the median in Figure 8c to be close to 0 with a small IQR, indicating little to no bias between our estimates. We find a median value of 0.76 mm/yr, and an IQR of 4.55 mm/yr, indicating a high degree of scatter around the median.

We then assess whether there is any correlation between rate differences and rate magnitudes, which could arise if the velocity reference frames between systems have slightly different scales. Figure 8d provides a test of this hypothesis. The median value, which may be interpreted as an estimate of the scale factor transformation between the GPS and GDD velocity reference frames, is 1.05 (regardless of inclusion of the outliers), very close to the value of 1.0 we would expect if the velocity reference frames were identical. The IQR of the rate ratios is 2.76.

A significant takeaway from our analysis above derives from the simplest of our rate parameter explorations and is independent of the GDD rate estimates: GPS stations located less than 50 km from one another exhibit vertical rate differences of up to 4.48 ± 0.78 mm/yr, which is over 4 times the average GPS vertical rate uncertainty (Table 2). This result suggests that the GPS rate uncertainties are a major factor in the residual rates apparent in GPD-GDD time series but permits no conclusion regarding the accuracy of GDD-derived rate estimates. Longer GPS time series may result in more precise determination of vertical rate, which might reduce peak to peak variation (Figures S1–S4). Future analyses of GPS and GDD rate estimates should explore this possibility.

4.5. Amplitude of Annual and Semiannual Seasonal Motions

The amplitudes of the annual components of the seasonal cycles associated with the best fit models to the GPS and GDD time series are plotted in Figure 9. Like Figure 6, Figure 9 reveals similar spatial distributions between annual amplitudes estimated by GPS and GDD. The highest amplitudes are located near the Amazon river where mass load variations are known to be high (Bevis et al., 2005) and the lowest amplitudes are further away. The weighted basin-wide average annual amplitude is 10.29 ± 0.92 mm for GDD and 10.18 ± 0.76 mm for GPS, with a combined weighted basin average of both GPS and GDD of 10.22 ± 0.57 mm.

Differencing the GPS and GDD annual amplitude estimates (Figure 10a) results in a median annual amplitude of 3.00 mm, which is 72% lower than the median annual amplitude of GPS (10.70 mm). Both GPS and GDD have a similar degree of scatter. The total range and IQR of GPS annual amplitudes are 23.93 mm (including NAUS) and 5.30 mm, respectively, and the total range and IQR of GDD annual amplitudes are 21.55 and 7.41 mm, respectively. After subtracting GDD from GPS, the total range drops to 5.80 mm and the IQR is 1.37 mm, which represent reductions by 76% and 74% relative to GPS. Differencing GPS and GDD estimates brings the median value and ranges of the GPS-GDD time series closer to the zero value we would expect if GDD captured all of the seasonal motion observed using GPS.

In Figure 10b, we plot GDD and GPS annual amplitudes against one another. We observe a moderately high degree of correlation between the two data sets, as indicated by the r^2 value of 0.78. Moreover, the y intercept

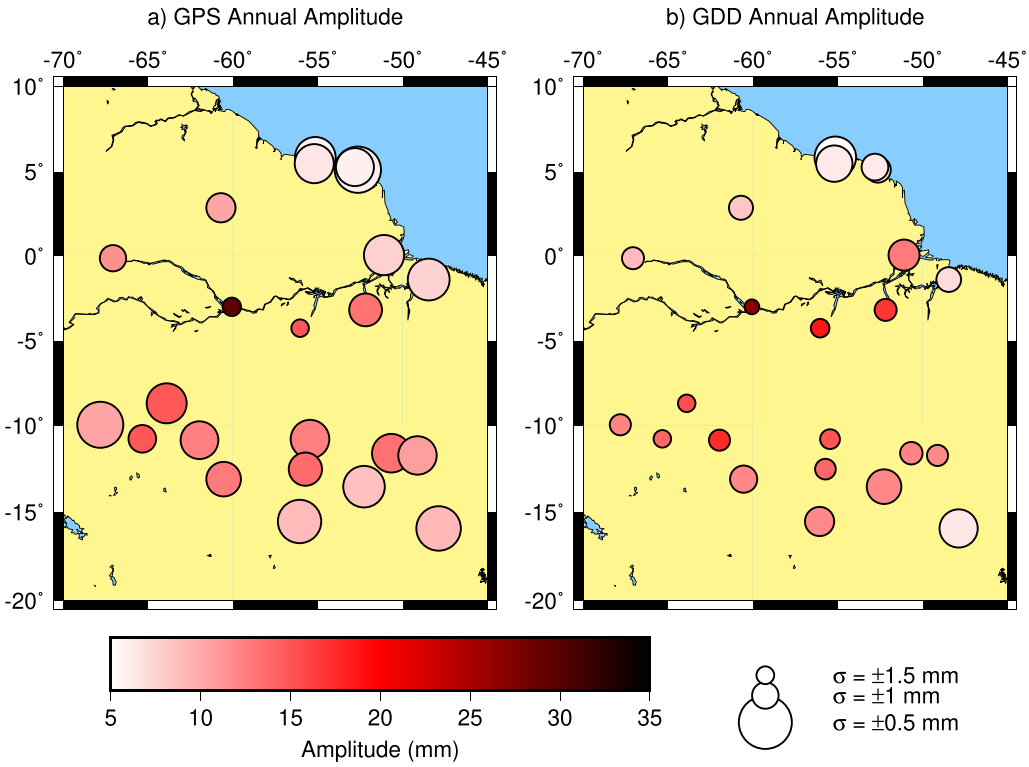

Figure 9. Spatial distribution across the Amazon basin of the annual amplitude of the seasonal cycle for (a) GPS and (b) GDD. Circle colors indicate the magnitude of amplitude. The size of the circles is inversely proportional to the uncertainties associated with the estimate; larger circles indicate smaller uncertainties.

of the best fit line is close to zero, with a slope of 0.95 ± 0.04, indicating that GDD accounts for a large portion of the annual signal observed using GPS. Since the slope is less than 1.0, it suggests that there may be a slight scale difference between the two data sets.

The Bland-Altman difference plot of Figure 10c shows that in subtracting GDD annual amplitudes from GPS annual amplitudes, the median of the resulting values is −0.44 mm. There is virtually no correlation between the GPS-GDD differences and mean annual amplitudes. The IQR of 3.63 mm is reasonably small given the large annual amplitudes found for both GPS and GDD, but the IQR is large relative to the average annual amplitude uncertainty of $\leq\sim$ 2 mm (Table 2). This might be expected given that some stations are closer to the river, where the hydrologic load is larger, and others are further from the river. In Figure 10d the median of the ratios is approximately 0.96, consistent with the slope of the line in Figure 10b. The median value of the data in Figure 10d is fairly well constrained, as the range of the ratios is 0.83, and the IQR is only 0.28.

Although the Bland-Altman plots in Figures 10c and 10d suggest a small apparent scale difference also identified in Figure 10b, this apparent scaling is not reflected in the vertical rate or, as we will discuss in the next paragraph, semiannual amplitudes. Because the kinematic model with which we have fit the time series is linear in the model parameters, we would expect the scale to affect all of the parameters equally. Unequal scaling between GPS and GDD model parameters may be the result of local or equipment-related effects on GPS station observations. However, our analysis of the concatenated GPS residuals earlier in this section suggests that the noise processes are relatively similar from station to station. It is thus possible that the range in observed scale factors is a symptom of the small number of data upon which our study and previous studies have been based or perhaps is an indication that we have slightly underestimated the uncertainties in our parameter estimates. Future work might explore this apparent scale factor using a larger number of stations and longer time series.

In Figure 11a, the median of GPS semiannual amplitudes is 1.76 mm, with a range of 3.25 mm and an IQR of 0.72‘mm. The median of GDD semiannual amplitudes is 2.02 mm, with a range of 1.98 mm and an IQR

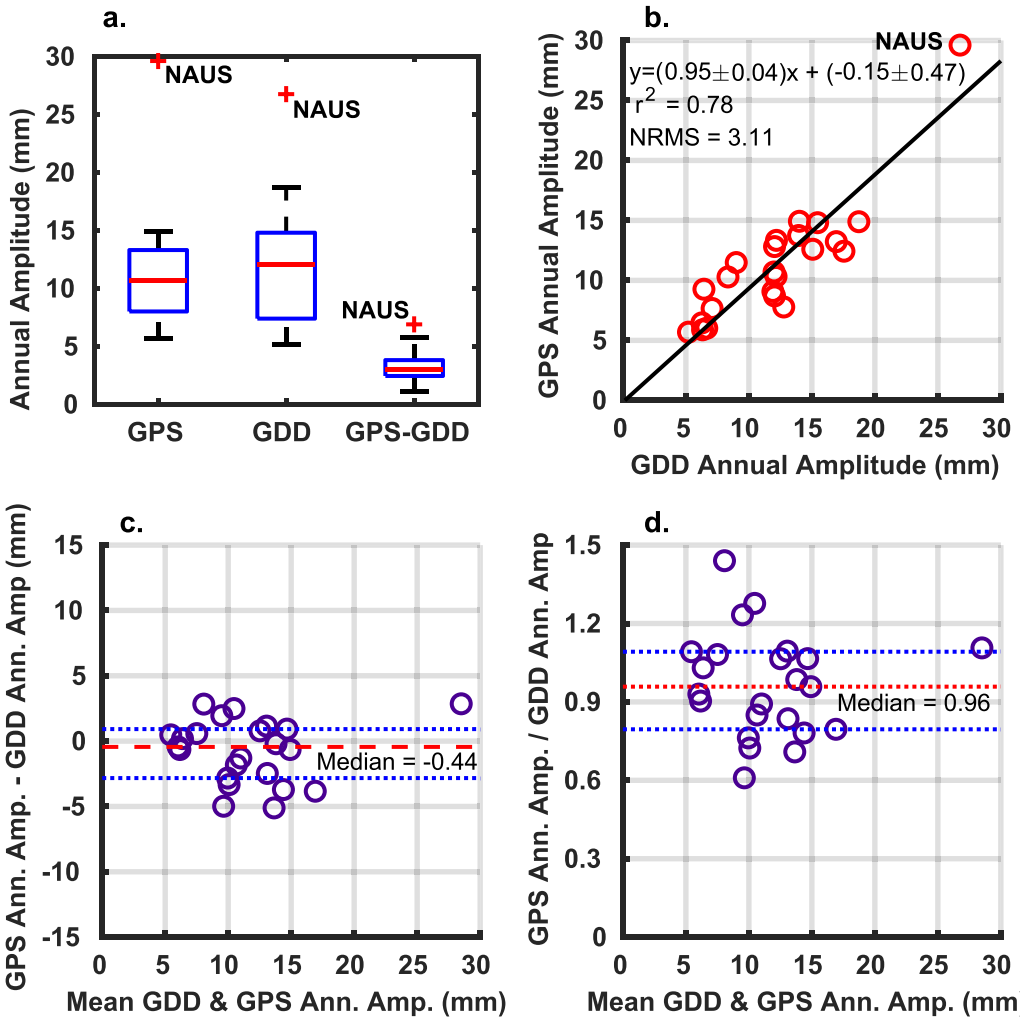

Figure 10. (a) Three boxplots of the annual amplitudes found using the time series of (1) GPS, (2) GDD, and (3) GPS-GDD residuals. In this plot, the red plus sign indicates NAUS, a statistical outlier. Again, outliers are defined as data that are 3 IQRs below the first quartile or 3 IQRs above the third quartile. The calculated residuals in boxplot (3) include NAUS. (b) A scatter plot comparing GPS annual amplitude with GDD annual amplitude at all 23 GPS stations. A weighted (by uncertainties in both GPS and GDD) best fit line is plotted as a solid line, and the equation of the line is displayed. NAUS is labeled but is not considered an outlier for this graph. (c) Bland-Altman plot with the mean of GPS and GDD annual amplitudes on the *x* axis and difference between them on the *y* axis. The dashed red horizontal line represents the median of the differences. Two blue horizontal dotted lines denote the location of the first and third quartiles of the data. (d) Bland-Altman plot with mean of GPS and GDD annual amplitudes on the *x* axis and ratio of the annual amplitudes (GPS/GDD) on the *y* axis. The dotted lines represent the first and third quartiles, and the dashed line represents the median of the ratios.

of 0.82 mm. These values are all in relative agreement. However, when the GDD time series are subtracted from the GPS time series, the resulting GPS-GDD time series actually has a larger range (2.21 mm), median (1.91 mm), and IQR (1.01 mm). While we might have expected a decrease in semiannual amplitude after subtracting GDD from the GPS time series, instead, we find an increase in semiannual amplitude in the residual time series.

We investigate this issue further in Figure 11b. There is essentially no correlation ($r^2 = 0.02$) between the GPS and GDD semiannual amplitude estimates. We also plot the Bland-Altman difference in Figure 11c. Scatter among the differences exhibits a total range of 2.91 mm and an IQR of 1.01 mm, focused around the median value of −0.08 mm, suggesting little to no bias between the two estimate sets. There is also a low degree of correlation between the differences and the mean semiannual amplitudes. Further support for agreement between GPS and GDD semiannual amplitudes is offered in the Bland-Altman ratio plot of

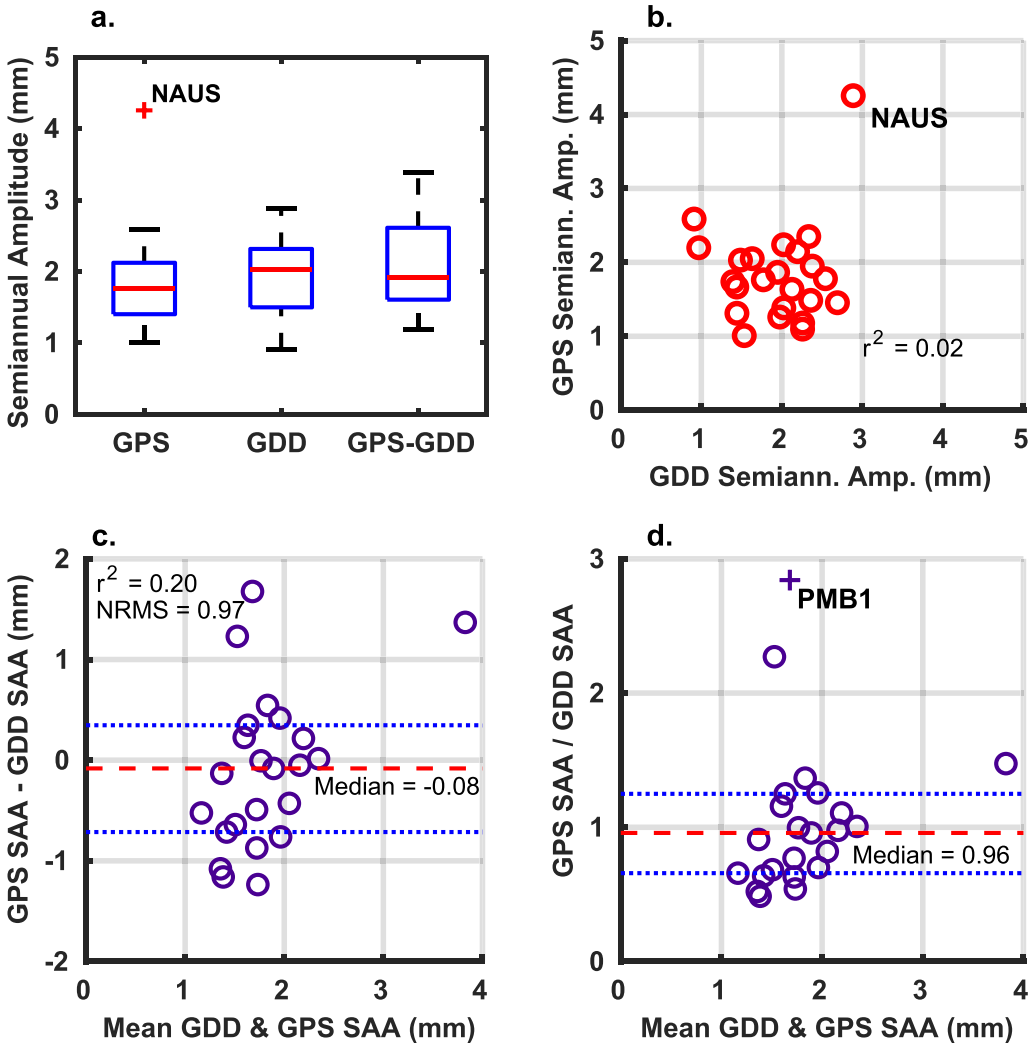

Figure 11. (a) Three boxplots of the semiannual amplitudes found using the time series of (1) GPS, (2) GDD, and (3) GPS-GDD residuals. The red plus sign here indicates NAUS. The calculated residuals include NAUS. (b) A scatter plot comparing GPS semiannual amplitude with GDD semiannual amplitude at all 23 GPS stations. The r^2 value between the data is 0.02. NAUS is labeled but is not considered an outlier for this graph. (c) Bland-Altman plot with the mean of GPS and GDD semiannual amplitudes on the x axis and difference between them on the y axis. The dashed red horizontal line represents the median of the differences. Two blue horizontal dotted lines denote the location of the first and third quartiles of the data. The NRMS value of the residuals and the r^2 value are placed at the top of the plot. (d) Bland-Altman plot with mean of GPS and GDD semiannual amplitudes on the x axis and ratio of the annual amplitudes (GPS/GDD) on the y axis. The blue dotted lines represent the first and third quartiles, and the red dashed line represents the median of the ratios.

Figure 11d, where the ratios of GPS to GDD semiannual amplitudes are plotted against the mean rate. The median of these ratios is 0.96, which suggests little or no small systematic scaling between the two systems. Additionally, the IQR is low at 0.56, if we do not omit the outlier. We also obtain a range that is not much larger, 2.36 (again, not omitting the outlier).

Despite finding some evidence for agreement between GPS and GDD semiannual amplitudes in Figures 11c and 11d, Figure 11a shows that subtracting the GDD time series from the GPS time series produces no reduction in the median semiannual amplitude. This may indicate a difference in the phase of the semiannual amplitudes inferred by GPS and GDD. It is unlikely that such a phase difference is due to a viscoelastic response to loading at some of the GPS stations, since we do not see the same phase difference in the annual amplitudes. Instead, it may be because of the relative sensitivity of the GPS stations to where the loading is located in the Amazon basin. For example, heavy flooding in the west may not fully appear in the loading

signal as viewed by GPS to the east until days, weeks, or months later. This effect may also be seen in the GDD signal, as we discuss in the next section, but it may not be as sensitive as GPS to these mass loading delays due to its large spatial resolution.

5. Implications for GPS, GRACE, and the Amazon Basin

Between March 2011 and November 2016, the Amazon basin, in part or in whole, experienced several monthlong episodes of both extreme flooding and extreme drought. The extreme flooding of 2011–2012 was characterized by heavy rainfall in the north-northwest of the Amazon basin, beginning around November 2011 (Espinoza et al., 2012). At almost every station in our study, there is a distinct subsidence signal in Spring 2012, coincident with the peak of the wet season at those stations, and influenced by the arrival of flood discharge. The next event of note is the 2013–2014 flood. This occurred mainly in the southwestern Amazon, with anomalously high precipitation starting in September 2013, intensifying in January 2014 and causing record flooding in February 2014 (Espinoza et al., 2014).

Also within this time frame (March 2011 to November 2016), there was a strong El Niño event from 2015 to 2016, which produced record-breaking drought conditions over much of the Amazon basin. Our supposition that these extreme weather events affect the displacement signal in GPS and GRACE is supported when we look at the time series residuals (Figure 12). The hydrological drought of the 2015–2016 El Niño was between October 2015 and July 2016 (Yang et al., 2018). Stations NAUS, PAIT, and ROJI have a distinct positive displacement anomaly between October 2015 and July 2016 in both GPS and GDD time series, indicating exceptional drying (Figure 12). One aspect of the 2015–2016 El Niño event is that drought conditions were not evenly distributed across the basin. In fact, Jiménez-Muñoz et al. (2016) show that while the east to northeast Amazon basin was experiencing extreme drought, the west to southwest was experiencing normal to unusually wet conditions.

The basin-wide weighted average of both GPS and GDD annual amplitudes is 10.22 ± 0.57 mm, which conveys the large seasonal changes in hydrologic and atmospheric mass loading. The flooding and drought events of the Amazon basin produce even larger anomalies. The 2015–2016 El Niño produced an anomalously high peak for that years' dry season in GPS and GDD at nearly all of the stations in our analysis. The effects of this event are significantly reduced by subtracting GDD from GPS. If we had used a simple kinematic model to reduce the GPS time series, instead of displacements estimated from GRACE, such an event would not have been well modeled. This leads to an unrealistic determination of the error spectrum.

Our results carry significant implications for the Amazon basin. We calculated the weighted average of the vertical rates for the GPS and GDD time series with hydrologic loading only (Table S2). If this weighted average (1.27 ± 0.25) represents the average vertical rate for the region outlined in Figure 1 between March 2011 and November 2016, it would indicate an average net loss of approximately 6.2 Gt of water per year. Put another way, the eastern Amazon basin lost approximately 2.5 million Olympic-sized swimming pools of water per year. When a major carbon sink like the Amazon basin loses water so drastically, it increases the risk of forest fires. When wildfires ravage the rainforest, carbon dioxide is released into the atmosphere and causes an immediate decrease in rainfall (Langenbrunner et al., 2018). Following the fire, the carbon dioxide that the rainforests would otherwise absorb contributes to increasing global temperatures. These higher temperatures then lead to drought, which leads to wildfire, and so on in a positive feedback loop that could accelerate destruction of the Amazon and its fragile ecosystems.

In our noise processes analysis, we confirmed that GRACE has exceptional utility in accounting for some of the vertical signals in GPS. The κ of the concatenated GPS residual time series is -1.2759 ± 0.0007, representing fractional Brownian motion. In subtracting GDD from GPS, the κ of the concatenated residual time series was reduced to -0.3346 ± 0.0006, which indicates fractional Gaussian noise and is closer to representing a white noise process. This reduction of power at low frequencies indicates that some of the temporal variation observed in GPS and GDD residual time series is correlated between measurement systems. This is a strong indication that this variation is caused by changes in mass loading that are not accounted for by secular or periodic motions alone.

Our results also have significant implications for the future of GPS coordinate time series analyses. Correlated noise in GPS, thought to be the product of inherent station performance issues, may be partly rooted in unaccounted for changes in mass loading over time. Removing the mass loading signal from GPS using

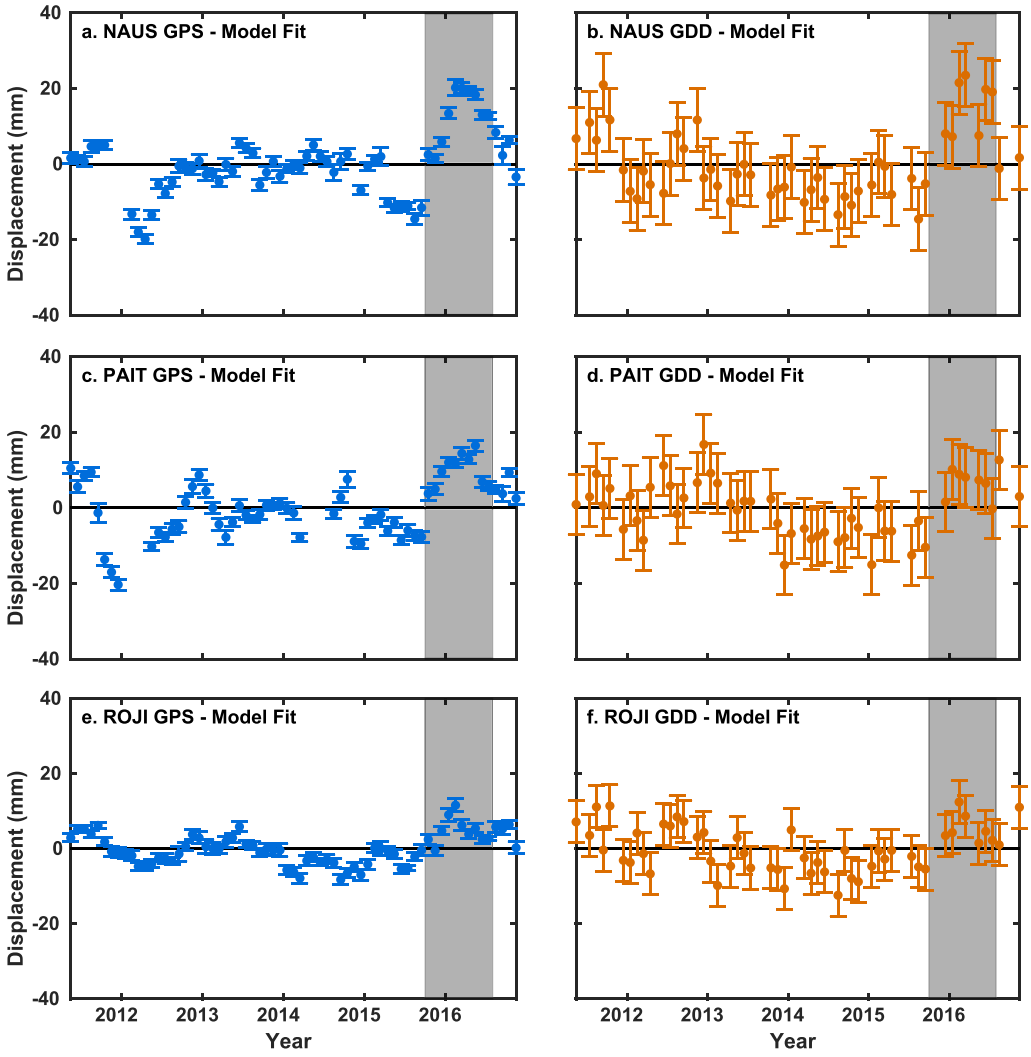

Figure 12. Three sets of plots displaying time series residuals (observations minus model fit) for GPS and GDD. Plots (a) and (b) are data from station NAUS, (c) and (d) are from station PAIT, and (e) and (f) are from station ROJI. The approximate time period of hydrologic drought in the Amazon basin is represented by the gray bar, which extends from 1 October 2015 to 31 July 2016.

GDD in future studies may provide more accurate estimates of crustal deformation due to tectonics. Moreover, Fu et al. (2012) and Fu et al. (2013) have shown that GRACE can estimate horizontal displacements with high accuracy. Further investigations should determine the degree to which GRACE can account for correlated noise in the horizontal components of GPS coordinate time series. Additionally, future studies should also repeat this comparison of GPS and GDD in regions with smaller seasonal mass loading signals and fewer extreme weather events.

6. Conclusion

GPS and GDD have the potential to provide complementary information about mass loading and to enhance further understanding of the GPS error spectrum. Used together in an analysis of deformation associated with changes in mass loading, they have the potential to provide more robust results than using one or the other separately. Here we have identified the level of agreement between GPS and GDD time series of displacement. We have identified components of the mass load deformation field that are not well characterized by secular trends and periodic annual and semiannual motions.

We compared the observed displacements from GPS coordinate time series and the displacements estimated from GRACE geopotential fields. We looked at the differences between vertical rate and seasonal amplitudes

to determine the degree to which GPS and GDD agree. Using Bland-Altman difference and ratio diagrams, we assessed that the spatial agreement between GPS and GDD is substantial and shows little bias and only a marginally different scale between measurement systems.

We also found evidence that both systems record correlated subseasonal to multiyear signals. Subtracting GDD from GPS modifies the GPS error spectrum, flattening it at low frequencies into the fractional Gaussian noise regime. We anticipate that this finding may provide an impetus for future studies of the GPS error spectrum to consider mass loading as a source of reddened spectra that has been reported previously. Even studies of non-loading-induced crustal deformation should consider the impacts of mass loading signals in the vertical or horizontal motions of GPS, since mass load signals are likely to bias estimates for secular motion if unaccounted for.

Acknowledgments
We thank the Nevada Geodetic Laboratory for providing precise coordinate time series data for GPS stations around the world. All time series analysis was performed using the Hector software developed by Machiel Bos at Universidade de Beira Interior, Portugal. GRACE data are freely available from the NASA Physical Oceanography Distributed Active Archive Center (PODAAC). C. H. acknowledges support from the TRIFF-WEES program at the University of Arizona. The code used to analyze GRACE data in this work is available freely online (Harig & Simons, 2015). Installation instructions for the various Slepian code repositories can be found online (https://doi.org/10.5281/zenodo.583624). The code used to perform all other analyses is available online (https://doi.org/10.5281/zenodo.3571429). This manuscript was substantially improved based on the constructive comments of Adrian Borsa, Associate Editor Paul Tregoning, and an anonymous reviewer.

References

Argus, D. F., Fu, Y., & Landerer, F. W. (2014). Seasonal variation in total water storage in California inferred from GPS observations of vertical land motion. *Geophysical Research Letters*, *41*, 1971–1980. https://doi.org/10.1002/2014GL059570

Bennett, R. A. (2008). Instantaneous deformation from continuous GPS: Contributions from quasi-periodic loads. *Geophysical Journal International*, *174*(3), 1052–1064. https://doi.org/10.1111/j.1365-246X.2008.03846.x

Bevis, M., Alsdorf, D., Kendrick, E., Fortes, L. P., Forsberg, B., Smalley Jr, R., & Becker, J. (2005). Seasonal fluctuations in the mass of the Amazon River system and Earth's elastic response. *Geophysical research letters*, *32*, L16308. https://doi.org/10.1029/2005GL023491

Bevis, M., Wahr, J., Khan, S. A., Madsen, F. B., Brown, A., & Willis, M. (2012). Bedrock displacements in Greenland manifest ice mass variations, climate cycles and climate change. *Proceedings of the National Academy of Sciences of the United States of America*, *109*(30), 11,944–11,948. https://doi.org/10.1073/pnas.1204664109

Bland, J. M., & Altman, D. G. (1986). Statistical methods for assessing agreement between two methods of clinical measurement. *Lancet*, *327*(8476), 307–310. https://doi.org/10.1016/S0140-6736(86)90837-8

Blewitt, G., Hammond, C., & Kreemer, C. (2018). Harnessing the GPS data explosion for interdisciplinary science. *Eos*, *99*, 1–2. https://doi.org/10.1029/2018EO104623

Bogusz, J., & Klos, A. (2016). On the significance of periodic signals in noise analysis of GPS station coordinates time series. *GPS Solutions*, *20*(4), 655–664. https://doi.org/10.1007/s10291-015-0478-9

Borsa, A. A., Agnew, D. C., & Cayan, D. R. (2014). Ongoing drought-induced uplift in the western United States. *Science*, *345*, 1587–1590. https://doi.org/10.1126/science.1260279

Bos, M., Fernandes, R., Williams, S., & Bastos, L. (2013). Fast error analysis of continuous GNSS observations with missing data. *Journal of Geodesy*, *87*(4), 351–360. https://doi.org/10.1007/s00190-012-0605-0

Cheng, M., Tapley, B. D., & Ries, J. C. (2013). Deceleration in the Earth's oblateness. *Journal of Geophysical Research: Solid Earth*, *118*, 740–747. https://doi.org/10.1002/jgrb.50058

Davis, J. L., Elósegui, P., Mitrovica, J. X., & Tamisiea, M. E. (2004). Climate-driven deformation of the solid Earth from GRACE and GPS. *Geophysical Research Letters*, *31*, L24605. https://doi.org/10.1029/2004GL021435

Espinoza, J. C., Marengo, J. A., Ronchail, J., Carpio, J. M., Flores, L. N., & Guyot, J. L. (2014). The extreme 2014 flood in south-western Amazon basin: The role of tropical-subtropical South Atlantic SST gradient. *Environmental Research Letters*, *9*(12), 124007. https://doi.org/10.1088/1748-9326/9/12/124007

Espinoza, J. C., Ronchail, J., Guyot, J. L., Junquas, C., Drapeau, G., & Martinez, J. M. (2012). From drought to flooding: Understanding the abrupt 2010–11 hydrological annual cycle in the Amazonas River and tributaries. *Environmental Research Letters*, *7*(2), 024008. https://doi.org/10.1088/1748-9326/7/2/024008

Farrell, W. E. (1972). Deformation of the Earth by surface loads. *Reviews of Geophysics*, *10*(3), 761–797. https://doi.org/10.1029/RG010i003p00761

Fu, Y., Argus, D. F., Freymueller, J. T., & Heflin, M. B. (2013). Horizontal motion in elastic response to seasonal loading of rain water in the Amazon Basin and monsoon water in Southeast Asia observed by GPS and inferred from GRACE. *Geophysical Research Letters*, *40*, 6048–6053. https://doi.org/10.1002/2013GL058093

Fu, Y., & Freymueller, J. T. (2012). Seasonal and long-term vertical deformation in the Nepal Himalaya constrained by GPS and GRACE measurements. *Journal of Geophysical Research*, *117*, B03407. https://doi.org/10.1029/2011JB008925

Fu, Y., Freymueller, J. T., & Jensen, T. (2012). Seasonal hydrological loading in southern Alaska observed by GPS and GRACE. *Geophysical Research Letters*, *39*(15), 1–5. https://doi.org/10.1029/2012GL052453

Gloor, M., Brienen, R. J., Galbraith, D., Feldpausch, T., Schöngart, J., Guyot, J. L., & Phillips, O. (2013). Intensification of the Amazon hydrological cycle over the last two decades. *Geophysical Research Letters*, *40*, 1729–1733. https://doi.org/10.1002/grl.50377

Gu, Y., Yuan, L., Fan, D., You, W., & Su, Y. (2017). Seasonal crustal vertical deformation induced by environmental mass loading in mainland China derived from GPS, GRACE and surface loading models. *Adv. Space Res.*, *59*(1), 88–102. https://doi.org/10.1016/j.asr.2016.09.008

Harig, C., & Simons, F. J. (2012). Mapping Greenland's mass loss in space and time. *Proceedings of the National Academy of Sciences of the United States of America*, *109*(49), 24–27. https://doi.org/10.1073/pnas.1206785109

Harig, C., & Simons, F. J. (2015). Accelerated West Antarctic ice mass loss continues to outpace East Antarctic gains. *Earth and Planetary Science Letters*, *415*, 134–141. https://doi.org/10.1016/j.epsl.2015.01.029

Harig, C., & Simons, F. J. (2016). Ice mass loss in Greenland, the Gulf of Alaska, and the Canadian Archipelago: Seasonal cycles and decadal trends. *Geophysical Research Letters*, *43*, 3150–3159. https://doi.org/10.1002/2016GL067759

Hayes, G. P., Meyers, E. K., Dewey, J. W., Briggs, R. W., Earle, P. S., & Benz, H. M. (2017). *Tectonic summaries of magnitude 7 and greater earthquakes from 2000 to 2015*. Reston, VA: US Geological Survey. 2016–1192.

Herring, T. A., Melbourne, T. I., Murray, M. H., Floyd, M. A., Szeliga, W. M., King, R. W., & Wang, L. (2016). Plate boundary observatory and related networks: GPS data analysis methods and geodetic products. *Reviews of Geophysics*, *54*(4), 759–808. https://doi.org/10.1002/2016RG000529

Jiménez-Muñoz, J. C., Mattar, C., Barichivich, J., Santamaría-Artigas, A., Takahashi, K., Malhi, Y., & Van Der Schrier, G. (2016). Record-breaking warming and extreme drought in the Amazon rainforest during the course of El Niño 2015–2016. *Scientific Reports*, *6*, 33130. https://doi.org/10.1038/srep33130

Jin, S., & Zhang, T. (2016). Terrestrial water storage anomalies associated with drought in southwestern USA from GPS observations. *Surveys in Geophysics*, *37*(6), 1139–1156. https://doi.org/10.1007/s10712-016-9385-z

Kanda, R. V., & Simons, M. (2010). An elastic plate model for interseismic deformation in subduction zones. *Journal of Geophysical Research*, *115*, B03405. https://doi.org/10.1029/2009JB006611

Landerer, F. W., & Swenson, S. (2012). Accuracy of scaled GRACE terrestrial water storage estimates. *Water resources research*, *48*, W04531.

Langbein, J. (2004). Noise in two-color electronic distance meter measurements revisited. *Journal of Geophysical Research*, *109*, B04406. https://doi.org/10.1029/2003JB002819

Langenbrunner, B., Pritchard, M., Kooperman, G. J., & Randerson, J. T. (2018). Why does Amazon precipitation decrease when tropical forests respond to increasing CO_2? *Earth's Future*, *7*(4), 450–468. https://doi.org/10.1029/2018EF001026

Lenton, T. M., Held, H., Kriegler, E., Hall, J. W., Lucht, W., Rahmstorf, S., & Schellnhuber, H. J. (2008). Tipping elements in the Earth's climate system. *Proceedings of the National Academy of Sciences of the United States of America*, *105*(6), 1786–1793. https://doi.org/10.1073/pnas.0705414105

Mandelbrot, B. B., & Van Ness, J. W. (1968). Fractional Brownian motions, fractional noises and applications. *SIAM Review*, *10*(4), 422–437. https://doi.org/10.1137/1010093

Moreira, D. M., Calmant, S., Perosanz, F., Xavier, L., Rotunno Filho, O. C., Seyler, F., & Monteiro, A. C. (2016). Comparisons of observed and modeled elastic responses to hydrological loading in the Amazon basin. *Geophysical Research Letters*, *43*, 9604–9610. https://doi.org/10.1002/2016GL070265

Nahmani, S., Bock, O., Bouin, M. N., Santamaría-Gómez, A., Boy, J. P., Collilieux, X., & Wppelmann, G. (2012). Hydrological deformation induced by the West African Monsoon: Comparison of GPS, GRACE and loading models. *Journal of Geophysical Research*, *117*, B05409. https://doi.org/10.1029/2011JB009102

Pan, Y., Shen, W. B., Hwang, C., Liao, C., Zhang, T., & Zhang, G. (2016). Seasonal mass changes and crustal vertical deformations constrained by GPS and GRACE in Northeastern Tibet. *Sensors-Switzerland*, *16*(8), 1221. https://doi.org/10.3390/s16081211

Simons, F. J., & Dahlen, F. A. (2006). Spherical Slepian functions and the polar gap in geodesy. *Geophysical Journal International*, *166*(3), 1039–1061. https://doi.org/10.1111/j.1365-246X.2006.03065.x

Steckler, M. S., Nooner, S. L., Akhter, S. H., Chowdhury, S. K., Bettadpur, S., Seeber, L., & Kogan, M. G. (2010). Modeling Earth deformation from monsoonal flooding in Bangladesh using hydrographic, GPS, and Gravity Recovery and Climate Experiment (GRACE) data. *Journal of Geophysical Research*, *115*, B08407. https://doi.org/10.1029/2009JB007018

Swenson, S., Chambers, D., & Wahr, J. (2008). Estimating geocenter variations from a combination of GRACE and ocean model output. *Journal of Geophysical Research*, *113*, B08410. https://doi.org/10.1029/2007JB005338

Tapley, B. D., Bettadpur, S., Ries, J. C., Thompson, P. F., & Watkins, M. M. (2004). GRACE measurements of mass variability in the Earth system. *Science*, *305*(5683), 503–505. https://doi.org/10.1126/science.1099192

Tregoning, P., Watson, C., Ramillien, G., McQueen, H., & Zhang, J. (2009). Detecting hydrologic deformation using GRACE and GPS. *Geophysical Research Letters*, *36*, L15401. https://doi.org/10.1029/2009GL038718

Tukey, J. W. (1977). Some thoughts on clinical trials, especially problems of multiplicity. *Science*, *198*(4318), 679–684. https://doi.org/10.1126/science.333584

Van Camp, M., Métivier, L., De Viron, O., Meurers, B., & Williams, S. (2010). Characterizing long-time scale hydrological effects on gravity for improved distinction of tectonic signals. *Journal of Geophysical Research*, *115*, B07407. https://doi.org/10.1029/2009JB006615

van Dam, T., Wahr, J., & Lavallée, D. (2007). A comparison of annual vertical crustal displacements from GPS and Gravity Recovery and Climate Experiment (GRACE) over Europe. *Journal of Geophysical Research*, *112*, B03404. https://doi.org/10.1029/2006JB004335

Wahr, J., Molenaar, M., & Bryan, F. (1998). Time variability of the Earth's gravity field: Hydrological and oceanic effects and their possible detection using GRACE. *Journal of Geophysical Research*, *103*(B12), 30,205–30,229. https://doi.org/10.1029/98JB02844

Watkins, M. M., Wiese, D. N., Yuan, D. N., Boening, C., & Landerer, F. W. (2015). Improved methods for observing Earth's time variable mass distribution with GRACE using spherical cap mascons. *Journal of Geophysical Research: Solid Earth*, *120*, 2648–2671. https://doi.org/10.1002/2014JB011547

Wiese, D. N., Landerer, F. W., & Watkins, M. M. (2016). Quantifying and reducing leakage errors in the JPL RL05M GRACE mascon solution. *Water Resources Research*, *52*, 7490–7502. https://doi.org/10.1002/2016WR019344

Williams, S. (2003). The effect of coloured noise on the uncertainties of rates estimated from geodetic time series. *Journal of Geodesy*, *76*, 483–494. https://doi.org/10.1007/s00190-002-0283-4

Wu, X., Heflin, M. B., Ivins, E. R., Argus, D. F., & Webb, F. H. (2003). Large-scale global surface mass variations inferred from GPS measurements of load-induced deformation. *Geophysical Research Letters*, *30*(14), 1742. https://doi.org/10.1029/2003GL017546

Yang, J., Tian, H., Pan, S., Chen, G., Zhang, B., & Dangal, S. (2018). Amazon drought and forest response: Largely reduced forest photosynthesis but slightly increased canopy greenness during the extreme drought of 2015/2016. *Global Change Biology*, *24*(5), 1919–1934. https://doi.org/10.1111/gcb.14056